JPhys Energy

PAPER • OPEN ACCESS

Charge transport modelling of perovskite solar cells accounting for non-Boltzmann statistics in organic and highly-doped transport layers

To cite this article: Will Clarke *et al* 2023 *J. Phys. Energy* **5** 025007

Journal of Physics: Energy

PAPER

Charge transport modelling of perovskite solar cells accounting for non-Boltzmann statistics in organic and highly-doped transport layers

Will Clarke[1,*], Matthew J Wolf[2,3], Alison Walker[3] and Giles Richardson[1]

[1] Mathematical Sciences, University of Southampton, Southampton, United Kingdom
[2] Institute of Physical Chemistry, RWTH Aachen, Germany
[3] Department of Physics, University of Bath, Bath, United Kingdom
* Author to whom any correspondence should be addressed.

E-mail: wc3g16@soton.ac.uk

Keywords: perovskite solar cells, drift-diffusion, transport layers, statistical models, organic semiconductors

OPEN ACCESS

RECEIVED
6 February 2023

REVISED
8 March 2023

ACCEPTED FOR PUBLICATION
16 March 2023

PUBLISHED
27 March 2023

Abstract

We present a drift–diffusion model of a perovskite solar cell (PSC) in which carrier transport in the charge transport layers (TLs) is not based on the Boltzmann approximation to the Fermi–Dirac (FD) statistical distribution, in contrast to previously studied models. At sufficiently high carrier densities the Boltzmann approximation breaks down and the precise form of the density of states function (often assumed to be parabolic) has a significant influence on carrier transport. In particular, parabolic, Kane and Gaussian models of the density of states are discussed in depth and it is shown that the discrepancies between the Boltzmann approximation and the full FD statistical model are particularly marked for the Gaussian model, which is typically used to describe organic semiconducting TLs. Comparison is made between full device models, using parameter values taken from the literature, in which carrier motion in the TLs is described using (I) the full FD statistical model and (II) the Boltzmann approximation. For a representative TiO_2/MAPI/Spiro device the behaviour of the PSC predicted by the Boltzmann-based model shows significant differences compared to that predicted by the FD-based model. This holds both at steady-state, where the Boltzmann treatment overestimates the power conversion efficiency by a factor of 27%, compared to the FD treatment, and in dynamic simulations of current–voltage hysteresis and electrochemical impedance spectroscopy. This suggests that the standard approach, in which carrier transport in the TLs is modelled based on the Boltzmann approximation, is inadequate. Furthermore, we show that the full FD treatment gives a more accurate representation of the steady-state performance, compared to the standard Boltzmann treatment, as measured against experimental data reported in the literature for typical TiO_2/MAPI/Spiro devices.

1. Introduction

Over the past decade, perovskite solar cells (PSCs) have seen rapid developments, in both efficiency and stability, to an extent that they are now viewed as a realistic prospective next-generation photovoltaic technology. However despite the impressive efficiency of modern PSCs (the current record for certified power conversion efficiency (PCE) is 25.7% [1]), challenges remain that must be overcome to enable large-scale commercial manufacture of perovskite solar panels, the chief amongst these being their relatively poor long-term stability and the presence of lead in the perovskite structure. An increased understanding of the fundamental materials and device physics governing their properties and performance will be key to the further development of PSC technology. In this context, modelling plays a central role in elucidating the basic physical processes underlying the performance of PSCs. In particular, drift–diffusion modelling, which provides a macroscopic description of an entire cell, and directly links to the properties of the materials from which it is constructed, has proven to be a powerful tool to understand PSC device physics [2–4]. PSCs typically use a planar architecture in which a perovskite absorber layer is sandwiched between a highly

n-doped electron transport layer (ETL) and a highly p-doped hole transport layer (HTL). While some drift–diffusion models comprising **only** electrons and holes continue to be published [5–7], it has repeatedly been shown that migration of ion vacancies is not only present in the perovskite layer but vital to understanding their operation [8–10]. These simplistic models, which omit ion migration, are incapable of replicating the dynamic current–voltage or impedance responses of PSCs [2, 8, 11–14]. The transport layers (TLs) are chosen such that light can enter through one of them, either the ETL (standard architecture) [15] or the HTL (inverted architecture) [16]. While early drift–diffusion models of PSCs omitted the TLs, focusing on the interplay between electronic and ionic conduction in the perovskite layer [8, 17–19], state of the art models include an explicit description of all three layers [12, 20–22], enabling a number of studies of the important role played by the TLs, and their interplay with the perovskite layer. Such studies have included investigations of the role of intrinsic materials properties, such as band alignment, carrier mobility [23] and dielectric constants [20], as well as extrinsic properties such as layer thickness [24] and doping densities [20], in determining both steady state [23, 24] and transient [20] cell characteristics.

As with any mathematical model, there are a number of assumptions and approximations that are made in the derivation of the drift–diffusion equations (see, e.g. [25]). In particular, and as will be discussed in detail in section 2, it is typically assumed that the diffusion coefficient (D) is related to the mobility (μ) via the classical Einstein relation (CER):

$$qD = \mu k_{\mathrm{B}} T;$$

this assumption is equivalent to the assumption that the carrier density is **sufficiently low** that the FD statistical distribution is well approximated by a Boltzmann distribution (see section 2). When this is not the case, the generalised Einstein relation (GER) must be used instead [26, 27]:

$$qD_{\mathrm{n}} = \mu_n n \frac{\partial E_{\mathrm{f}_n}}{\partial n}, \quad qD_{\mathrm{p}} = -\mu_p p \frac{\partial E_{\mathrm{f}_p}}{\partial p},$$

in which $E_{\mathrm{f_n}}$ and $E_{\mathrm{f_p}}$ are the electron and hole quasi-Fermi levels, respectively. This leads to more complex versions of the drift–diffusion equations, the functional forms of which depend on the density of states of the material, and which are, in general, no longer analytic. Physically, this results in an enhancement of the diffusion coefficient relative to the value from the CER, that increases with the local carrier density [27, 28]. Additionally, it is often assumed implicitly that the mobilities (μ_{n} and μ_{p}) do not depend on the carrier density. Some studies [29, 30] contradict this but the functional form of the dependence of mobility on carrier density is still debated [31]. Henceforth, for simplicity, we treat the mobilities as constants.

Tessler and Vaynzof have investigated the validity of the Boltzmann approximation in describing electronic carriers in the perovskite layer of a PSC, assuming a density of states function derived from a parabolic dispersion model, and concluded that, while the approximation is warranted in many scenarios, it can lead to appreciable errors in others [2]. However, conditions under which it is valid are likely to be more limited for the TLs than the perovskite layer for at least the following three reasons: (i) while the perovskite layer is undoped, the TLs tend to be heavily doped in order to increase their equilibrium carrier density (and hence also conductivity); (ii) even if the equilibrium carrier density in the bulk of the TL is sufficiently low for the Boltzmann approximation to be valid, much higher carrier densities can arise in the regions close to the interfaces between layers [20], or when the device is out of equilibrium; and (iii) as will be discussed in section 3, the range of carrier densities for which the Boltzmann approximation is valid depends strongly on the density of states (DoS) function of the material in question. The physical processes occurring at the material interfaces between the perovskite and the TLs have been shown to be highly important in explaining the dynamic behaviour of the cell, such as current–voltage hysteresis [32–35] and electrochemical impedance spectroscopy (IS) [32]. Point (ii) therefore leads us to conjecture that models based on the Boltzmann approximation in the TLs are not always appropriate when investigating the dynamic behaviour of PSCs. With reference to point (iii), disordered organic semiconductors, which are often used as one of the TLs in PSCs, are best described by a Gaussian DoS [36, 37], which is only accurately approximated by the Boltzmann distribution in a far smaller domain than inorganic materials with band structures described by a parabolic DoS [38]. The potential inaccuracies arising from the assumption of the CER have also been recognised by Abdel *et al* [39, 40] but only addressed for ion vacancies in the perovskite layer, rather than the carriers in the TLs.

In light of the above discussion, the purpose of this contribution is to investigate the effects of full Fermi–Dirac (FD) statistics in drift–diffusion models of PSC devices, with a particular focus on the TLs. We note that the three-layer drift–diffusion model is sufficiently complex that it is difficult to predict, without the aid of a full numerical solution of the model, exactly how errors associated with employing the Boltzmann approximation in one of the TLs might manifest themselves in the predicted device behaviour in

any particular scenario. For example, the accumulation of carriers near the perovskite interface is dependent on the distribution of ion vacancies in the perovskite, which itself is dependent on many material parameters as well as external conditions, such as temperature, light intensity, and applied voltage [20]. Here we shall present example numerical results for a typical three layer device. In particular, we compare the prediction made using a model in which carrier transport in the TLs is described using full FD statistics to one in which carrier transport in the TLs is described using the Boltzmann approximation. Since we consider only a single typical device there remains room for further investigation for other device configurations.

The remainder of the paper is organised as follows. We begin, in section 2 by discussing the drift-diffusion equations in which carrier transport is modelled using (i) the Boltzmann approximation and (ii) full FD statistics. We further show that the application of full FD statistics causes a density-dependent diffusivity enhancement (equivalent to the GER), the form of which is determined by the DoS function. Then, in section 3, we consider the form of the DoS function for both ordered inorganic and disordered organic materials, and show that the choice of DoS function must be carefully considered in scenarios for which the Boltzmann approximation does not hold. The range of carrier densities for which Boltzmann statistics accurately approximate full FD statistics is discussed for a variety of relevant TL materials in section 4. In section 5, comparisons are made between the predictions of a device-level model of a PSC in which charge carrier motion in the TLs is modelled by (i) the Boltzmann approximation and (ii) full FD statistics. The results obtained using these two different descriptions of the TLs are compared for both steady state performance and transient measurements, namely current–voltage hysteresis and IS. Finally, we draw our conclusions in section 6.

2. The drift–diffusion equations and the GER

The basis of the drift–diffusion model is a set of conservation equations, one for each particle species, in which the change in the particle number density is driven by the net flux into a region and contributions from volume source and sink terms. In most photovoltaic devices the only particle species modelled by the drift–diffusion equations are the charge carriers, i.e. electrons in the conduction band (volume density n) and holes in the valence band (volume density p). The source and sink terms in the corresponding conservation equations model photogeneration and recombination, respectively. In halide perovskites it is also necessary to model the transport of one or more mobile point defect species, such as charged anion or cation vacancies [8]. However, it is usually assumed that any defects/dopants in the charge TLs, which are our focus here, are static and homogeneously distributed.

In one dimension, the case to which we restrict ourselves here, the electron and hole conservation equations take the form

$$\frac{\partial n}{\partial t} = \frac{1}{q}\frac{\partial j^n}{\partial x} + G(x,t) - R(n,p), \tag{1a}$$

$$\frac{\partial p}{\partial t} = -\frac{1}{q}\frac{\partial j^p}{\partial x} + G(x,t) - R(n,p), \tag{1b}$$

in which $G(x,t)$ and $R(n,p)$ are the rates of generation and recombination of electron–hole pairs per unit volume, respectively, and j^{n} and j^{p} are the electron and hole current densities, respectively. The latter are calculated from the carrier densities and the quasi-Fermi levels via the relations

$$j^{\mathrm{n}} = \mu_{\mathrm{n}} n \frac{\partial E_{\mathrm{f_n}}}{\partial x}, \tag{2a}$$

$$j^{\mathrm{p}} = \mu_{\mathrm{p}} p \frac{\partial E_{\mathrm{f_p}}}{\partial x}, \tag{2b}$$

where μ_{n} and μ_{p} are the electron and hole mobilities, while $E_{\mathrm{f_n}}$ and $E_{\mathrm{f_p}}$ are the quasi-Fermi levels of the electrons in the conduction band and holes in the valence band, respectively. The implicit assumption made in using quasi-Fermi levels to characterise the state of the semiconductor is that the valence band electrons are (locally) in thermal equilibrium with each other and that the conduction band electrons are (locally) in thermal equilibrium with each other, but that valence and conduction band electrons are not necessarily in thermal equilibrium with each other. Constitutive equations that relate the quasi-Fermi levels to n, p and ϕ, and which derive from the statistical distributions of the electrons in the valence and conduction bands, must also be specified. The system of drift-diffusion equations is closed by Poisson's equation for the electric potential ϕ,

$$\frac{\partial^2 \phi}{\partial x^2} = -\frac{\rho}{\varepsilon}, \tag{3}$$

where $\rho = q(p - n)$ is the net charge density and ε is the permittivity of the material.

The quasi-Fermi levels depend on the carrier density and the electric potential as follows:

$$E_{\mathrm{f_n}} = F_{\mathrm{n}}(n, T) - q\phi, \tag{4a}$$

$$E_{\mathrm{f_p}} = F_{\mathrm{p}}(p, T) - q\phi, \tag{4b}$$

where $F_{\mathrm{n,p}}$ are functions that depend on both the band structure and the statistical distribution, the forms of which shall be derived below. The current densities (2) can thus be split into a diffusion term and a drift term, as follows:

$$j^{\mathrm{n}} = \mu_{\mathrm{n}} n \frac{\partial E_{\mathrm{f_n}}}{\partial n}\frac{\partial n}{\partial x} - q\mu_{\mathrm{n}} n \frac{\partial \phi}{\partial x}, \tag{5a}$$

$$j^{\mathrm{p}} = \mu_{\mathrm{p}} p \frac{\partial E_{\mathrm{f_p}}}{\partial p}\frac{\partial p}{\partial x} - q\mu_{\mathrm{p}} p \frac{\partial \phi}{\partial x}. \tag{5b}$$

We define the chemical diffusivities of electrons and holes, respectively, according to Fick's law,

$$qD_{\mathrm{n}} = \mu_{\mathrm{n}} n \frac{\partial E_{\mathrm{f_n}}}{\partial n}, \tag{6a}$$

$$qD_{\mathrm{p}} = -\mu_{\mathrm{p}} p \frac{\partial E_{\mathrm{f_p}}}{\partial p}, \tag{6b}$$

where the change in sign between the electron and hole diffusivities is due to the sign of their respective charges. This result, referred to as the GER [26, 27], allows the current equations to be written as

$$j^{\mathrm{n}} = qD_{\mathrm{n}}\frac{\partial n}{\partial x} - q\mu_{\mathrm{n}} n \frac{\partial \phi}{\partial x}, \tag{7a}$$

$$j^{\mathrm{p}} = -qD_{\mathrm{p}}\frac{\partial p}{\partial x} - q\mu_{\mathrm{p}} p \frac{\partial \phi}{\partial x}. \tag{7b}$$

When the conduction electrons and valence holes satisfy Boltzmann statistics (as is frequently assumed in semiconductor modelling [2, 41–45]), the dependencies of the QFLs on carrier density (i.e. the $F_{\mathrm{n,p}}$ functions in equations (4)) are logarithmic (a result that will be derived in the following sections). In such scenarios it is straightforward to show that the GER is replaced by the CER,

$$qD_{\mathrm{n,p}} = \mu_{\mathrm{n,p}} k_{\mathrm{B}} T, \tag{8}$$

in which the ratio of diffusivity to mobility is constant, i.e. not dependent on the local carrier concentration. While this approximation greatly simplifies the model, the accuracy of the CER is often poor (as will be shown). In such scenarios the full GER is required.

2.1. Statistical integrals and the Fermi level

In order to determine equations for the electron and hole current currents from (2), expressions for the quasi-Fermi levels in terms of the carrier densities are required. In thermal equilibrium, the probability (f) that an electronic state with energy E is occupied in a material with Fermi level E_{f} is given by the FD statistical distribution,

$$f(E; E_{\mathrm{f}}) = \frac{1}{\exp\left(\frac{E - E_{\mathrm{f}}}{k_{\mathrm{B}} T}\right) + 1} \tag{9}$$

where T is temperature and k_{B} is Boltzmann's constant. The density (per unit volume) of electrons lying in the conduction band with energies between E and $E + \mathrm{d}E$ is therefore given by the product of the FD distribution, f, and the DoS (per unit volume), or DoS, $\hat{g}(E)\mathrm{d}E$. The corresponding density of holes in the valence band is given by the product of $(1 - f)$ with the DoS in the valence band $\hat{g}(E)\mathrm{d}E$.

Under the assumption that the material is a semiconductor, we first split the DoS $\hat{g}(E)$ into that pertaining to the valence band $\hat{g}_{\mathrm{v}}(E)$ and that pertaining to the conduction band $\hat{g}_{\mathrm{c}}(E)$ (see figure 1) and write

$$\hat{g}(E) = \hat{g}_{\mathrm{v}}(E) + \hat{g}_{\mathrm{c}}(E). \tag{10}$$

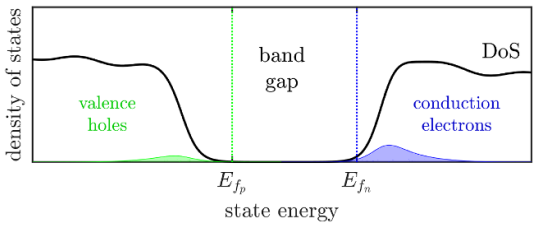

Figure 1. The filling of electron states. The solid black line shows the density of states (DoS) function $\hat{g}(E)$, solid coloured lines show the density of filled states per unit energy (specifically, $\hat{g}(E)f(E;E_{\mathrm{f_n}})$ for conduction electrons and $\hat{g}(E)[1-f(E;E_{\mathrm{f_p}})]$ for valence holes), and shaded areas show the total carrier density, integrated over all energies. Here the electron QFL is closer to the band edge than the hole QFL, meaning a higher density of electrons than holes.

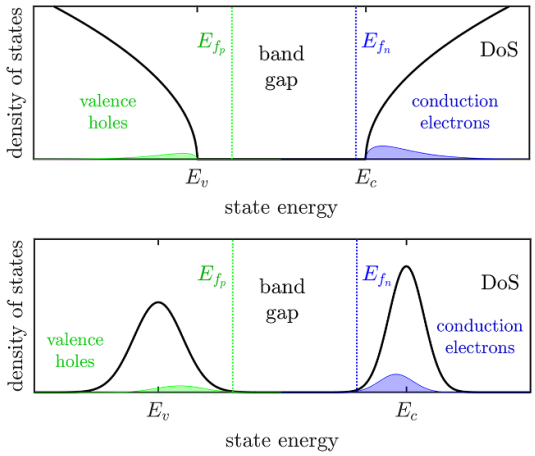

Figure 2. The filling of electron states in (top) parabolic and (bottom) Gaussian DoS functions.

It is usually assumed that the bands are perfectly distinct, meaning there exists a finite range of energies between the highest occupied state and the lowest unoccupied state at absolute zero in which the DoS is zero. However, in the case of organic semiconductors the bands do not have well-defined edges (see figure 2) and this can lead to definitions of $\hat{g}_{\mathrm{v}}(E)$ and $\hat{g}_{\mathrm{c}}(E)$ which are convenient, but for which there is some overlap of the tails of both functions. We assume that the bands have sufficient separation that any overlap in the DoS functions is negligible and note that any material that violates this would be a poor semiconductor. The total electron and hole densities (per unit volume) are thus

$$n = \int_{-\infty}^{\infty} f(E;E_{\mathrm{f_n}})\hat{g}_{\mathrm{c}}(E)\mathrm{d}E, \tag{11a}$$

$$p = \int_{-\infty}^{\infty} \left[1-f(E;E_{\mathrm{f_p}})\right]\hat{g}_{\mathrm{v}}(E)\mathrm{d}E, \tag{11b}$$

where the Fermi level E_{f} in the FD statistical distribution (9) is replaced by the QFL in the conduction/valence band in the expression for the electron/hole density.

For convenience, it is also assumed that the conduction and valence band DoS functions can each be cast in terms of (at least) two dimensional constants, an effective DoS (g_{c} or g_{v}) and reference energies E_{c} or E_{v}, corresponding to the conduction and valence band edges (in the case of inorganic semiconductors) and to the LUMO and HOMO (in the case of organic semiconductors). The dimensionless functions $\hat{N}_{\mathrm{c}}$ and $\hat{N}_{\mathrm{v}}$ are used to describe the general shape of the DoS function in the vicinity of the reference energies E_{c} and E_{v}, respectively. This allows us to write:

$$\hat{g}_{\mathrm{c}}(E) = \frac{g_{\mathrm{c}}}{k_{\mathrm{B}}T}\hat{N}_{\mathrm{c}}\left(\frac{E-E_{\mathrm{c}}}{k_{\mathrm{B}}T}\right), \tag{12a}$$

$$\hat{g}_{\mathrm{v}}(E) = \frac{g_{\mathrm{v}}}{k_{\mathrm{B}}T}\hat{N}_{\mathrm{v}}\left(-\frac{E-E_{\mathrm{v}}}{k_{\mathrm{B}}T}\right), \tag{12b}$$

where $\hat{N}_c$ and $\hat{N}_v$ are here referred to as reduced densities of states. These reduced DoS functions can be obtained from the DoS functions defined in (10) by inverting (12) to obtain

$$\hat{N}_c(\eta) = \frac{k_B T}{g_c} \hat{g}_c \left(E_c + k_B T \eta\right), \tag{13a}$$

$$\hat{N}_v(\eta) = \frac{k_B T}{g_v} \hat{g}_v \left(E_v - k_B T \eta\right), \tag{13b}$$

in which η can be interpreted as a dimensionless state energy level. With these DoS functions, and substituting the FD distribution (9), the electron and hole densities (11) become

$$n = g_c \int_{-\infty}^{\infty} \frac{1}{k_B T} \frac{\hat{N}_c\left(\frac{E-E_c}{k_B T}\right)}{1+\exp\left(\frac{E-E_{f_n}}{k_B T}\right)} \mathrm{d}E, \tag{14a}$$

$$p = g_v \int_{-\infty}^{\infty} \frac{1}{k_B T} \frac{\hat{N}_v\left(-\frac{E-E_v}{k_B T}\right)}{1+\exp\left(\frac{E_{f_p}-E}{k_B T}\right)} \mathrm{d}E. \tag{14b}$$

Carrier densities and quasi-Fermi levels are therefore related by an integral dependent on the reduced DoS. Specifically, the carrier densities are given by the expressions

$$n = g_c \mathcal{S}_c \left(\frac{E_{f_n} - E_c}{k_B T}\right), \tag{15a}$$

$$p = g_v \mathcal{S}_v \left(-\frac{E_{f_p} - E_v}{k_B T}\right), \tag{15b}$$

where the **statistical integrals**, $\mathcal{S}_c$ and $\mathcal{S}_v$, are the functions defined by the relations

$$\mathcal{S}_c(\xi) = \int_{-\infty}^{\infty} \frac{\hat{N}_c(\eta)}{1+\exp\left(\eta-\xi\right)} \mathrm{d}\eta, \tag{16a}$$

$$\mathcal{S}_v(\xi) = \int_{-\infty}^{\infty} \frac{\hat{N}_v(\eta)}{1+\exp\left(\eta-\xi\right)} \mathrm{d}\eta, \tag{16b}$$

in which ξ may be interpreted as a dimensionless QFL. We note that, in practice, ξ will almost always be negative, meaning both QFLs lie between the two reference energies, E_c and E_v, in the band gap. We invert these expressions (15) for the carrier densities to obtain expressions for the QFLs in terms of the densities. Substituting for the conduction band and valence band reference energies using $E_c = -E_a - q\phi$ and $E_v = -E_a - E_g - q\phi$, leads to the following expressions for the QFLs:

$$E_{f_n} = k_B T \mathcal{S}_c^{-1}\left(\frac{n}{g_c}\right) - E_a - q\phi, \tag{17}$$

$$E_{f_p} = -k_B T \mathcal{S}_v^{-1}\left(\frac{p}{g_v}\right) - E_a - E_g - q\phi, \tag{18}$$

where $\mathcal{S}^{-1}$ is the inverse of $\mathcal{S}$. Here E_a denotes the electron affinity, the difference between the conduction band reference energy and the vacuum level, and $E_g = E_c - E_v$ is the gap between the two bands' reference energies. Note that energies are defined relative to the vacuum level at $E = 0$ eV. In turn, the diffusion coefficients can be calculated as functions of mobility and carrier density from the GERs (6):

$$qD_n = \mu_n k_B T n \frac{\partial}{\partial n}\left(\mathcal{S}_c^{-1}\left(\frac{n}{g_c}\right)\right), \tag{19a}$$

$$qD_p = \mu_p k_B T p \frac{\partial}{\partial p}\left(\mathcal{S}_v^{-1}\left(\frac{p}{g_v}\right)\right). \tag{19b}$$

Equivalently, the expressions for the QFLs (17)–(18) can be substituted directly into the current density equations (2) to obtain the following expressions for the currents:

$$j^n = \mu_n k_B T \left(\Delta_n(n)\frac{\partial n}{\partial x} - \frac{qn}{k_B T}\frac{\partial \phi}{\partial x}\right), \tag{20a}$$

$$j^{\mathrm{p}} = -\mu_{\mathrm{p}} k_{\mathrm{B}} T \left(\Delta_{\mathrm{p}}(p) \frac{\partial p}{\partial x} + \frac{qp}{k_{\mathrm{B}} T} \frac{\partial \phi}{\partial x} \right), \tag{20b}$$

in which

$$\Delta_{\mathrm{n}}(n) = n \frac{\partial}{\partial n} \left(\mathcal{S}_{\mathrm{c}}^{-1} \left(\frac{n}{g_{\mathrm{c}}} \right) \right), \tag{21a}$$

$$\Delta_{\mathrm{p}}(p) = p \frac{\partial}{\partial p} \left(\mathcal{S}_{\mathrm{v}}^{-1} \left(\frac{p}{g_{\mathrm{v}}} \right) \right) \tag{21b}$$

are carrier density-dependent diffusion enhancement functions that approach 1 in the limit of low carrier density [46–50], as will be shown below.

2.2. The Boltzmann approximation and the CER

It is well known that the FD distribution (9) approaches the Boltzmann distribution,

$$f(E; E_{\mathrm{f}}) \sim \exp\left(-\frac{E - E_{\mathrm{f}}}{k_{\mathrm{B}} T} \right), \tag{22}$$

for energies significantly greater than the Fermi level, $(E - E_{\mathrm{f}})/k_{\mathrm{B}}T \gg 1$. Thus, for Fermi energies sufficiently far away from the reference energy of the DoS, the FD distribution (9) in the statistical integral can be approximated by a Boltzmann distribution (22), and the statistical integral (16) becomes

$$\mathcal{S}(\xi) \approx \int_{-\infty}^{\infty} \hat{N}(\eta) \exp(\xi - \eta) \, \mathrm{d}\eta, \tag{23}$$

which can be evaluated as

$$\mathcal{S}(\xi) \approx A \exp(\xi), \tag{24}$$

where

$$A = \int_{-\infty}^{\infty} \hat{N}(\eta) \exp(-\eta) \, \mathrm{d}\eta \tag{25}$$

is a scaling constant determined by the reduced DoS, which can readily be reabsorbed into an effective DoS constant. Specifically, this scaling constant is large if there is a high DoS at energies below the reference energy, i.e. the DoS has a tail, decaying into the band gap. This approximation, often referred to as the Boltzmann approximation, is valid when the QFL lies far inside the band gap, i.e. $\xi \ll -1$.

Thus, Boltzmann distributed carriers have an exponential statistical integral, regardless of DoS function, with inverse $\mathcal{S}^{-1}(x) = \ln(\frac{x}{A})$. This function can be differentiated exactly, leading to

$$\frac{\partial}{\partial n} \left(\mathcal{S}_{\mathrm{c}}^{-1} \left(\frac{n}{g_{\mathrm{c}}} \right) \right) = \frac{1}{n}, \tag{26a}$$

$$\frac{\partial}{\partial p} \left(\mathcal{S}_{\mathrm{v}}^{-1} \left(\frac{p}{g_{\mathrm{v}}} \right) \right) = \frac{1}{p}, \tag{26b}$$

and the diffusion enhancement functions (21) therefore become $\Delta \equiv 1$, thus recovering the CER from the generalised form.

This result is independent of the value of the constant A. The choice of DoS function is therefore unimportant when the Boltzmann approximation holds. If the approximation does not hold, however, the functional form of the DoS becomes significant and must be carefully considered. Furthermore, the choice of DoS affects the domain of carrier densities for which the Boltzmann approximation does hold, as will be discussed in section 4.

3. DoS functions and statistical integrals

A number of different materials have been used as TLs in PSCs, both inorganic and organic. Charge carrier conduction occurs via different basic mechanisms in the two classes of material (viz. inorganic and organic), which, in the present context, is important because it determines the model for the DoS that is appropriate for a given TL material.

Inorganic semiconductors are typically (poly)crystalline with electrons inhabiting delocalised Bloch (travelling) wave states, and the DoS is derived from the (quantum mechanical) dispersion relations of the bands of states. In contrast, electrons in organic materials occupy localised molecular orbitals, and their motion occurs via thermally activated hopping between molecules. In the latter case, a continuous DoS function arises from the (classical) disorder in the molecular arrangements, which causes variations in the energy of the molecular orbitals[4].

As we shall see, in the present context the most important distinction between the two scenarios is that the DoS in a crystalline (inorganic, in this case) material has a well defined minimum, while this is not the case for the amorphous (organic) materials. In this section, we will consider appropriate choices of the DoS function for both crystalline inorganic and amorphous organic materials.

3.1. Crystalline inorganic materials—Parabolic and simplified Kane models

As mentioned above, the dispersion relation in an inorganic material has a well defined minimum and maximum. The energy (E) of an electron in a state with wavevector ($\mathbf{k}$) near to the conduction band minimum (with energy E_c and wavevector $\mathbf{k}_c$) can be approximated by an expansion in powers of $|\mathbf{k}-\mathbf{k}_c|$ (see for example [27, 55]). Furthermore, we assume the band structure to be isotropic about this minimum, meaning the expansion depends only on the magnitude $k=|\mathbf{k}-\mathbf{k}_c|$, so that

$$E(k)=E_c+k\frac{\partial E}{\partial k}\Big|_{k=0}+\frac{k^2}{2}\frac{\partial^2 E}{\partial k^2}\Big|_{k=0}+\mathcal{O}(k^3). \tag{27}$$

As $k=0$ is the point at which the conduction band has a minimum, the first derivative in this expansion is necessarily zero. Furthermore, on defining the conduction band effective mass by

$$m_c^*=\frac{\hbar^2}{\frac{\partial^2 E}{\partial k^2}\Big|_{k=0}}, \tag{28}$$

the following expression for the electron energy is obtained:

$$E-E_c=\frac{\hbar^2}{2m_c^*}k^2. \tag{29a}$$

This is referred to as the parabolic band approximation [55]. Similarly, the dispersion relation in the vicinity of the valence band maximum is

$$E-E_v=-\frac{\hbar^2}{2m_v^*}k^2. \tag{29b}$$

Note that this approximation is based upon a band structure with well-defined valence and conduction band edges that is not found in disordered systems, hence its use is limited to crystalline inorganic materials. The DoS function is then derived according to [27]

$$g(E)=\frac{1}{\pi^2}k^2\frac{\mathrm{d}k}{\mathrm{d}E} \tag{30}$$

to obtain the DoS functions (as defined in (10)),

$$\hat{g}_c(E)=\frac{2g_c}{\sqrt{\pi}}\left(\frac{1}{k_BT}\right)^{\frac{3}{2}}\sqrt{E-E_c}\quad\text{for } E>E_c, \tag{31a}$$

[4] The scenarios described here are, of course, idealisations. Both organic and inorganic materials can exhibit varying degrees of disorder, and intermediate or mixed modes of transport and DoS functions [51–54].

near the conduction band minimum, and

$$\hat{g}_{\mathrm{v}}(E) = \frac{2g_{\mathrm{v}}}{\sqrt{\pi}}\left(\frac{1}{k_{\mathrm{B}}T}\right)^{\frac{3}{2}}\sqrt{E_{\mathrm{v}}-E} \quad \text{for } E < E_{\mathrm{v}}, \tag{31b}$$

near the valence band maximum. Thus the reduced DoS functions ($\hat{N}_{\mathrm{c}}$ and $\hat{N}_{\mathrm{v}}$, as defined in (13)) have the same form, i.e.

$$\hat{N}(\eta) = \begin{cases} 0 & \eta < 0 \\ \frac{2}{\sqrt{\pi}}\sqrt{\eta} & \eta \geqslant 0. \end{cases} \tag{32}$$

The statistical integral corresponding to this reduced DoS function is $\mathcal{S}_{\mathrm{c,v}}(\xi) = \mathcal{F}(\xi)$, where $\mathcal{F}$ follows from (16), and is

$$\mathcal{F}(\xi) = \int_0^\infty \frac{2}{\sqrt{\pi}}\frac{\sqrt{\eta}}{1+\exp(\eta-\xi)}\mathrm{d}\eta, \tag{33}$$

and is referred to as the Fermi–Dirac integral[5].

Further away from the band extrema, the parabolic approximation becomes increasingly inaccurate. States further from the band edge can be modelled by the simplified form of Kane's model for dispersion in III–V semiconductors [57–59], in which (29*a*) and (29*b*) are replaced by

$$(E-E_{\mathrm{c}})\left(1+\alpha_{\mathrm{c}}(E-E_{\mathrm{c}})\right) = \frac{\hbar^2}{2m_{\mathrm{c}}^*}k^2 \tag{34a}$$

$$(E-E_{\mathrm{v}})\left(1-\alpha_{\mathrm{v}}(E-E_{\mathrm{v}})\right) = -\frac{\hbar^2}{2m_{\mathrm{c}}^*}k^2 \tag{34b}$$

where α_{c} and α_{v} are two parameters that determine the degree of non-parabolicity. We note that the Kane model reduces to the parabolic model in the limit that α goes to zero. Once again, the DoS functions can be derived from (30) to obtain

$$\hat{g}_{\mathrm{c}}(E) = \frac{2g_{\mathrm{c}}}{\sqrt{\pi}}\left(\frac{1}{k_{\mathrm{B}}T}\right)^{\frac{3}{2}}\sqrt{(E-E_{\mathrm{c}})\left(1+\alpha_{\mathrm{c}}(E-E_{\mathrm{c}})\right)}\left(1+2\alpha_{\mathrm{c}}(E-E_{\mathrm{c}})\right), \tag{35a}$$

$$\hat{g}_{\mathrm{v}}(E) = \frac{2g_{\mathrm{v}}}{\sqrt{\pi}}\left(\frac{1}{k_{\mathrm{B}}T}\right)^{\frac{3}{2}}\sqrt{(E_{\mathrm{v}}-E)\left(1+\alpha_{\mathrm{c}}(E_{\mathrm{v}}-E)\right)}\left(1+2\alpha_{\mathrm{c}}(E_{\mathrm{v}}-E)\right). \tag{35b}$$

These Kane DoS functions lead to an altered reduced DoS function taking the place of (32):

$$\hat{N}(\eta) = \begin{cases} 0 & \eta < 0 \\ \frac{2}{\sqrt{\pi}}\sqrt{\eta(1+\alpha^*\eta)}(1+2\alpha^*\eta) & \eta \geqslant 0, \end{cases} \tag{36}$$

where $\alpha^* = \alpha k_{\mathrm{B}}T$ is the dimensionless non-parabolicity parameter. The statistical integrals for non-parabolic bands are therefore $\mathcal{S}_{\mathrm{c}}(\xi) = \mathcal{K}(\xi;\alpha_{\mathrm{c}}^*)$ for conduction electrons and $\mathcal{S}_{\mathrm{v}}(\xi) = \mathcal{K}(\xi;\alpha_{\mathrm{v}}^*)$ for valence holes, where $\mathcal{K}$ (which follows from (16)) is

$$\mathcal{K}(\xi;\alpha^*) = \int_0^\infty \frac{2}{\sqrt{\pi}}\frac{\sqrt{\eta(1+\alpha^*\eta)}(1+2\alpha^*\eta)}{1+\exp(\eta-\xi)}\mathrm{d}\eta, \tag{37}$$

and is referred to here as the Kane–Fermi integral. The non-parabolic DoS function (including the parabolic limit $\alpha \to 0$) and the resulting Kane–Fermi integral are plotted in figure 3. We note once again that the Kane model reduces to the parabolic model in the limit that $\alpha^* \to 0$, and that therefore the Kane–Fermi integral approaches the FD integral in the same limit,

$$\lim_{\alpha^*\to 0}\mathcal{K}(\xi;\alpha^*) = \mathcal{F}(\xi). \tag{38}$$

[5] Specifically, this is the Fermi–Dirac integral of order 1/2 [56]. Note that some definitions omit the prefactor.

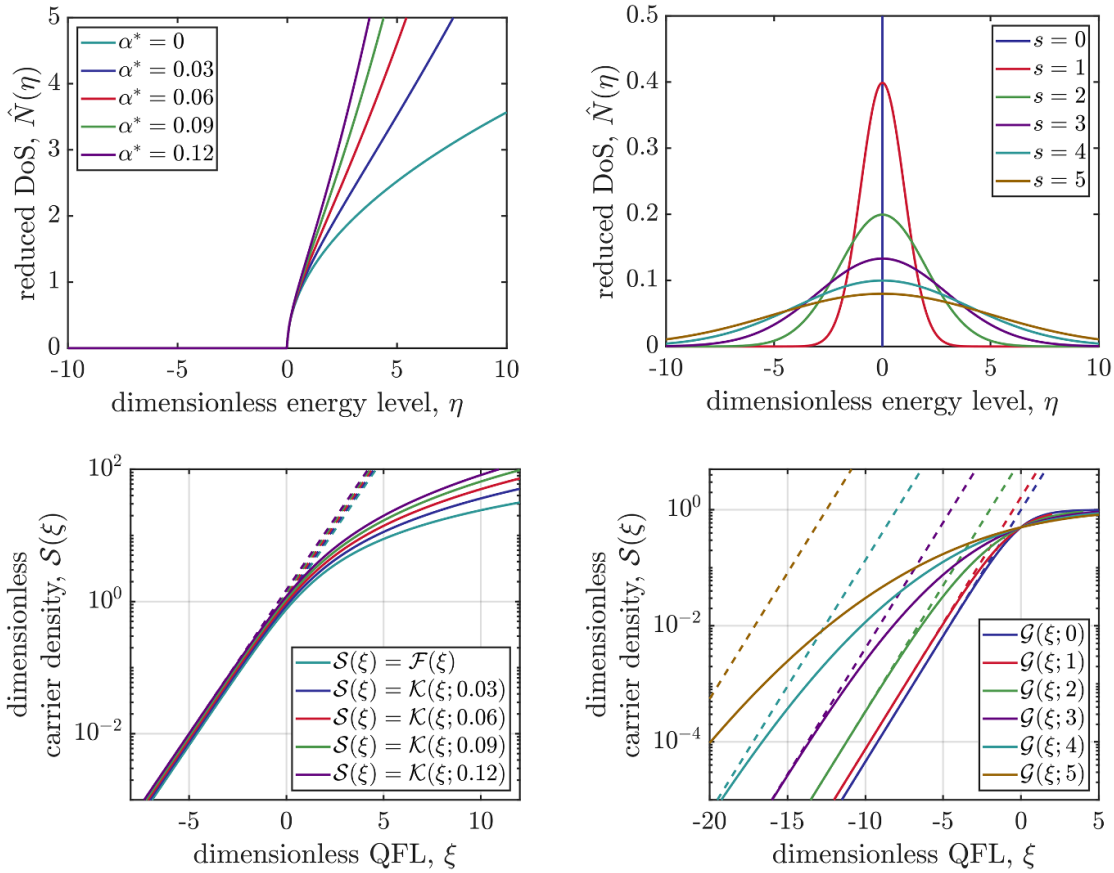

Figure 3. Reduced densities of state (top) and statistical integrals (bottom) derived from the simplified Kane dispersion (left) and Gaussian disorder (right) models. Solid lines in the bottom plots correspond to full FD distributions and dashed lines to Boltzmann distributions. Here, $\mathcal{F}, \mathcal{K}$, and $\mathcal{G}$ denote the Fermi–Dirac (33), Kane–Fermi (37), and Gauss–Fermi (41) integrals, α^* is the dimensionless non-parabolicity parameter of the Kane model and s is the dimensionless standard deviation of the Gaussian.

3.2. Amorphous organic materials—Gaussian model

The discrete transport sites in disordered organic materials are typically modelled by Gaussian DoS functions [36, 38], as represented in figure 2(b), of the form

$$\hat{g}_{\mathrm{c}}(E) = \frac{g_{\mathrm{c}}}{\sigma_{\mathrm{c}}\sqrt{2\pi}} \exp\left(-\frac{1}{2}\left(\frac{E - E_{\mathrm{c}}}{\sigma_{\mathrm{c}}}\right)^2\right), \tag{39a}$$

$$\hat{g}_{\mathrm{v}}(E) = \frac{g_{\mathrm{v}}}{\sigma_{\mathrm{v}}\sqrt{2\pi}} \exp\left(-\frac{1}{2}\left(\frac{E_{\mathrm{v}} - E}{\sigma_{\mathrm{v}}}\right)^2\right), \tag{39b}$$

where the degree of disorder is represented by the standard deviation, σ. Once again the reduced DoS functions ($\hat{N}_{\mathrm{c}}$ and $\hat{N}_{\mathrm{v}}$) can be obtained using (13) and have the form

$$\hat{N}(\eta, s) = \frac{1}{s\sqrt{2\pi}} \exp\left(-\frac{1}{2}\left(\frac{\eta}{s}\right)^2\right), \tag{40}$$

where $s = \frac{\sigma}{k_{\mathrm{B}}T}$ is the dimensionless disorder parameter, which in general differs between the 'conduction states' (for which the reduced DoS is $\hat{N}(\eta; s_{\mathrm{c}})$ and and 'valence states' (for which the reduced DoS is $\hat{N}(\eta; s_{\mathrm{v}})$. The crucial difference from the parabolic model is that the Gaussian band has no defined edge, meaning the reference energies E_{c} and E_{v} are now the band centres, the LUMO and HOMO energies, respectively. The statistical integrals (16) resulting from the Gaussian DoS are $\mathcal{S}_{\mathrm{c}}(\xi) = \mathcal{G}(\xi; s_{\mathrm{c}})$ for conduction electrons and $\mathcal{S}_{\mathrm{v}}(\xi) = \mathcal{G}(\xi; s_{\mathrm{v}})$ for valence holes, where $\mathcal{G}$ follows from (16):

$$\mathcal{G}(\xi; s) = \frac{1}{s\sqrt{2\pi}} \int_{-\infty}^{\infty} \frac{\exp\left(-\frac{1}{2}\left(\frac{\eta}{s}\right)^2\right)}{1 + \exp(\eta - \xi)} \mathrm{d}\eta, \tag{41}$$

and is referred to as the Gauss–Fermi integral [60]. The Gaussian DoS function and the resulting Gauss–Fermi integral are plotted in figure 3. Note that greater standard deviation effectively shifts the onset of the band further away from the reference energy, resulting in a shift in the statistical integral.

4. Accuracy of the Boltzmann approximation for common TL materials

As discussed in section 2.2, the CER is recovered from the general Einstein relation (GER) when carrier densities are sufficiently low so that the FD distribution (9) can be approximated by the Boltzmann distribution (22). Under this approximation, the statistical integrals take the form

$$\mathcal{S}(\xi) \approx A \exp(\xi), \qquad (24\ \textit{repeated})$$

where A is some constant determined by the functional form of the reduced DoS (25). For the Kane model (36), this constant is

$$A = \frac{1}{\sqrt{\pi\,\alpha^*}} \mathrm{e}^{\frac{1}{2\alpha^*}} K_2\left(\frac{1}{2\alpha^*}\right) \tag{42}$$

where K_2 is the second order modified Bessel function of the second kind (note that in the limit $\alpha^* \to 0$, the band becomes perfectly parabolic and $A \to 1$). The corresponding result in the Gaussian band model (40) is

$$A = \exp\left(\frac{s^2}{2}\right). \tag{43}$$

Notably, the CER is unaffected by the value of this constant, meaning that **the choice of DoS is unimportant when the Boltzmann approximation holds**. However, the functional form of the DoS does significantly affect the range of carrier densities in which the Boltzmann approximation holds. Furthermore, as the statistical integrals are not, in general, analytically invertible, the validity of the Boltzmann approximation for each band model usually has to be investigated numerically. In what follows, we conduct such an investigation for a number of different TL materials. In particular, we compute the diffusion enhancement factor Δ for some of the more commonly used TL materials in PSCs, noting that a value of Δ close to 1 implies that both the CER and the Boltzmann approximation accurately model the material's charge transport properties.

We consider the following inorganic TL materials: TiO_2, ZnO and SnO_2 (for the ETL) [61–65], and NiO (for the HTL) [66, 67]. In addition, we consider the following organic TL materials: spiro-MeOTAD [68, 69], PEDOT:PSS [70–72] and P3HT [73, 74] (for the HTL), and PCBM [75, 76] (for the ETL). More comprehensive lists of TL materials can be found in [77, 78] or through the Perovskite Database Project [79]. The relevant parameters for these TL materials, taken from the literature, are shown in table 1. We note that measurements of band nonparabolicity parameters in the literature are rare and, to the authors' knowledge, have not been reported for these materials, possibly because oxides are typically used as insulators in semiconductor applications. In the absence of measured values for inorganic TL materials, their bands will be assumed to be perfectly parabolic (i.e. $\alpha^* = 0$).

It is generally agreed that the Boltzmann approximation is sufficiently accurate for carriers in parabolic bands when the QFL is at least three thermal voltages from the band edge ($\xi < -3$), corresponding to carrier concentrations less than $0.05 g_{c,v}$. At this carrier density, the diffusion enhancement function, Δ, computed from from full FD statistics (and the GER), is approximately 1.018 and so is within 2% of the value given by the Boltzmann approximation (and the CER). For $\xi > -3$, however, the Boltzmann approximation to the FD integral begins to overestimate the carrier density, effectively allowing multiple carriers to occupy the same low-energy states. This can be seen in figure 3, where the FD integral is plotted with its Boltzmann approximation. The result is that the diffusion enhancement rapidly diverges from 1 as the carrier density exceeds $0.05 g_{c,v}$, as shown in figure 4.

Perhaps unexpectedly, the Boltzmann approximation to the Kane–Fermi integral is accurate over a wider range of densities for greater nonparabolicity. This is because the form of the reduced DoS means nonparabolicity increases the density of higher energy states, far away from the QFL, for the same effective DoS (shown in figure 3). Despite this, the deviation is minor and the CER can be considered accurate in the same domain as for perfectly parabolic bands.

Gaussian bands possess a tail of states extending into the band gap, as shown in figure 3. These states have energies closer to the QFL, meaning the Boltzmann approximation performs poorly. This is exacerbated by greater disorder [108], as seen in the dependence of the scaling constant for Gaussian bands (43) on the disorder, s. Consequently, the diffusion enhancement function, Δ, predicted by the Gauss-Fermi statistical

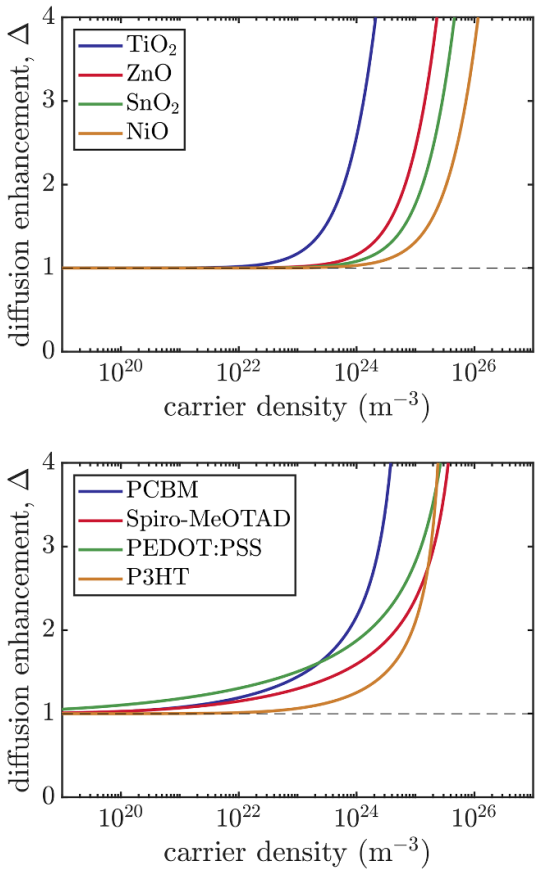

Figure 4. Diffusion enhancement functions according to the generalised Einstein relation for (top) inorganic and (bottom) organic transport layer materials. Δ is (21*a*) for ETL materials and (21*b*) for HTL materials. Similarly, carrier density is n for ETL materials and p for HTL materials. Parameters taken from table 1.

Table 1. Density of states parameters for common PSC transport layer materials. s is the dimensionless width of the Gaussian DoS, $s = \frac{\sigma}{k_B T}$.

Material	Layer	Record PCE (%)	$g_{c,v}$ (m^{-3})	$E_{c,v}$ (eV)	α^*
Inorganic					
NiO	HTL	20.68 [80]	1.1×10^{25} [81]	−5.41 [82]	N/A
TiO_2	ETL	24.8 [83]	2×10^{23} [81]	−4.13 [84]	N/A
ZnO	ETL	20.09 [85]	2.2×10^{24} [86]	−4.03 [87]	N/A
SnO_2	ETL	25.2 [88]	4.36×10^{24} [89]	−3.91 [90]	N/A
Organic					s
spiro-MeOTAD	HTL	25.2 [88]	1×10^{26} [91]	−5.09 [92]	3.38–4.08 [93–95]
PEDOT:PSS	HTL	21.15 [96]	1×10^{26} [97]	−5.13 [98]	4.09–5.08 [97, 99]
P3HT	HTL	23.9 [100]	4.2×10^{25} [101]	−4.7 [102]	1.04–3.12 [99, 101]
PCBM	ETL	21.43 [103]	$0.1-2\times10^{25}$ [104–106]	−3.95 [107]	2.81–5.38 [104, 105]

integral (and the equivalent GER) quickly diverges from 1 (i.e. from the value predicted by the Boltzmann approximation and the CER), as shown in figure 4. The greater the disorder of the material (i.e. the larger s is) the more rapid the divergence of Δ away from 1 as the concentration of electrons (or holes) is increased [28].

Measurements of the disorder parameter, s, for common organic PSC TL materials taken from the literature are shown in table 1. Values range from 1.04 to 5.38. The corresponding diffusion enhancement functions under the GER are plotted in figure 4. Even for the material with the least disorder (P3HT), the GER prediction of Δ has strongly diverged from 1 by the time the carrier density has increased to the typical TL doping density. This divergence is far more pronounced for the more disordered materials (such as PEDOT:PSS and PCBM) where it begins at relatively low carrier concentrations.

5. Effects of full FD statistics on device-level models

As discussed in the previous section, the diffusion enhancement predicted by charge transport models based upon a full description of the charge carrier statistics (i.e. using a full FD statistical model) is often significant in the materials commonly employed as TLs for PSCs over the range of carrier densities relevant to device operation. In this section, we examine the effect that this more complete physical description of the TLs has on the predictions of both steady-state and time-dependent device behaviour. In order to do this, we augment the widely-used model of the three-layer planar PSC [2, 12, 13, 19–21, 39, 109], with a model of carrier transport in the TLs based upon full FD statistics (i.e. (20)–(21)), to account for the fact that carrier densities are sufficiently high that the standard Boltzmann approximation breaks down in these layers. We define the statistical integrals as $\mathcal{S}_{\mathrm{E}}$ in the conduction band of the ETL and as $\mathcal{S}_{\mathrm{H}}$ in the valence band of the HTL, and note that the minority carriers in the TLs (i.e. holes in the ETL and electrons in the HTL) typically occur at such low densities that they do not significantly affect device behaviour, and so can be neglected. Since only a single significant carrier species is modelled in each TL, we drop the subscripts c and v that distinguish between conduction and valence bands.

The principle change to the standard device model, in which Boltzmann statistics are assumed accurate for all carriers, is that electron and hole current densities in the TLs are now computed with GERs, via (20)–(21), with an appropriate statistical model and material parameters. The changes to the statistical integrals also lead to minor alterations to the continuity and boundary conditions. These are described in more detail in [110] but the full drift–diffusion model solved here is also stated in appendix A.

The numerical results presented here are obtained using a recently released version of the open-source PSC simulation software, `IonMonger` [18, 21, 110], which enables the user to simulate a variety of measurement protocols, including current–voltage sweeps and IS. Details of the numerical methods used for adapting the discretised, non-dimensional charge transport model to account for the GER can be found in [110], along with a discussion of the challenges of implementing statistical integrals, which are neither analytically invertible nor differentiable, without significantly impacting the computation time.

The charge transport model of a PSC discussed here is too complex to easily predict how changes to the statistical models of the TLs affect the predictions of the cell's response to particular experimental protocols, but appropriate numerical solutions to the model allow us to investigate these changes on a case by case basis. In particular, they offer insight into the scenarios in which the error made by assuming Boltzmann statistics (and correspondingly the CER) leads to significant error in the predicted device behaviour.
In order to illustrate our hypotheses we compute solutions based on a representative data set for a TiO_2/MAPI/Spiro-MeOTAD cell (given in tables 2 and 3 of appendix B), with TL DoS parameters taken from table 1. We note that, while we construct the parameter set using material parameters taken from independent measurements, simulations using our parameter set may exhibit differences from the behaviour of a real device of this form as a consequence of device construction (e.g. material deposition method and architecture). The device considered here is intended to be representative, and a full parameter sweep lies outside the scope of this work.

5.1. Steady-state performance

Here the effect of the Boltzmann approximation in the TLs on four key performance parameters is investigated by computing numerical solutions to the drift–diffusion device model.

Steady-state results are shown in figures 5 and 6, in which direct comparison is made between the predictions of four key performance parameters (V_{OC}, J_{SC}, fill factor (FF), and PCE) obtained using full FD statistics in the TLs (i.e. the GER), and those obtained using the Boltzmann approximation (i.e. the CER). The short-circuit current (J_{SC}) shows the least sensitivity to the change in the statistical model of the TL carriers, a consequence of the low carrier densities in the TLs at this low voltage. Conversely, the predicted open-circuit voltage (V_{OC}) found using Boltzmann statistics is 9.43% greater than that found using the full statistical models of the TLs. This is a consequence of the Boltzmann approximation being far less accurate at open-circuit, where the large applied voltage leads to large carriers concentrations in the TLs. Combined with an increase in the FF, the increase in V_{OC} leads the model based on the Boltzmann approximation to significantly overestimate the PCE of the cell (by a factor of 27.04%). As shown in figure 5, where simulations are compared to data from the Perovskite Database Project [79], the simulated steady-state performance parameters obtained using simulations based on full FD statistics in the TLs are more representative of the experimental results found in the literature than those predictions made using simulations based on Boltzmann statistics for this particular device configuration.

The importance of these results lies in the fact that, owing to the difficulty in obtaining accurate estimates of material properties, many parameters are commonly fitted by comparing simulations to experiment, for

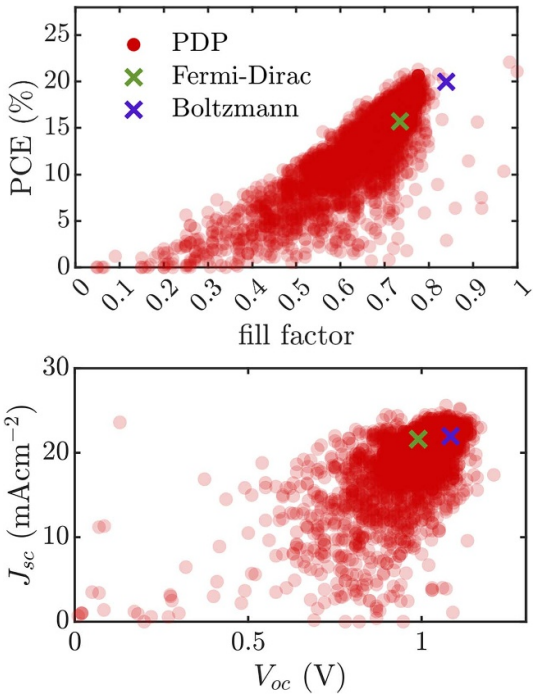

Figure 5. Measured steady state performance parameters of TiO_2/MAPI/Spiro-MeOTAD cells. Red circles were taken from The Perovskite Database Project [79]. Crosses were obtained through simulations using `IonMonger`, based on the parameter set given in appendix B. The band shapes in the TiO_2 and in the Spiro-MeOTAD were taken to be parabolic and Gaussian, respectively, using the parameters given in table 1. Significant differences can be observed between the predictions made using the Boltzmann approximation (blue crosses) and full Fermi–Dirac statistics (green crosses).

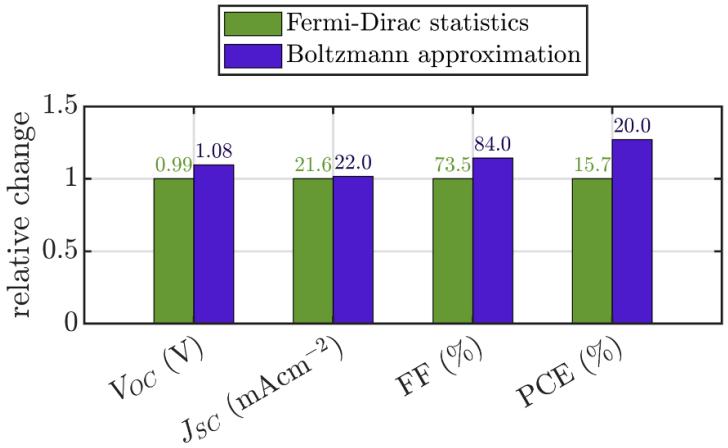

Figure 6. Sensitivity of key performance parameters to the Boltzmann approximation in the transport layers of a TiO_2/MAPI/Spiro-MeOTAD cell. Obtained through simulation using `IonMonger`. The parameter set is listed in appendix B. The band shapes in the TiO_2 and Spiro-MeOTAD were parabolic and Gaussian, respectively, with parameters taken from table 1.

values such as the short-circuit current and the open-circuit voltage. Thus, if the model predicts these values incorrectly (as seen here), material parameter estimates obtained through fitting will also be incorrect, leading to divergence between fitted parameter values obtained from the same material using different experimental protocols. This is likely to create confusion in the field and lead to difficulty in obtaining reliable and accurate material parameters estimates.

5.2. Current–voltage hysteresis

Differences in the predictions of PSC behaviour between models based on Boltzmann statistics in the TLs and those based on full FD statistics are not restricted to steady state behaviour. As shown in figures 7 and 8, simulations of J-V hysteresis and IS both show significant differences depending on which of these two modelling assumptions is applied.

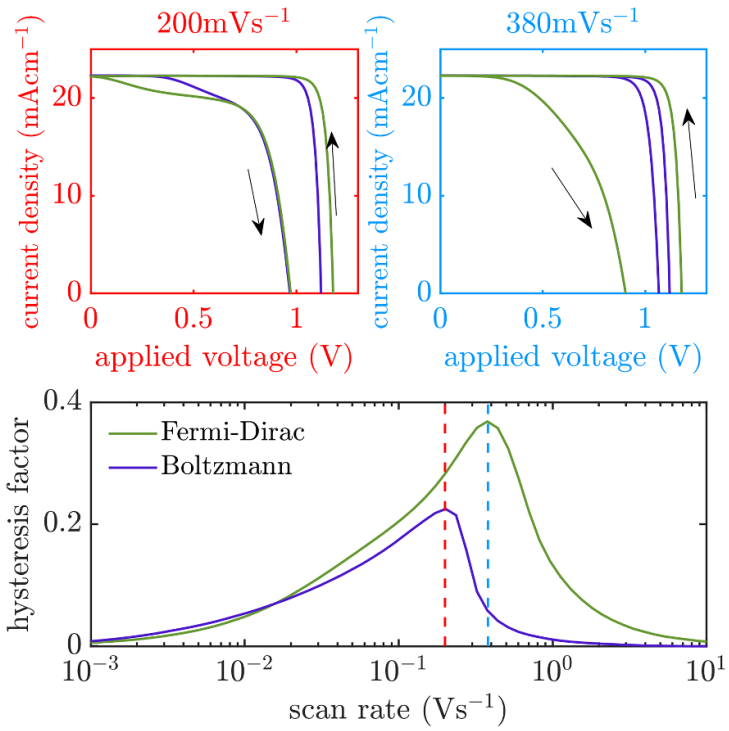

Figure 7. The effect of the Boltzmann approximation vs. full Fermi–Dirac statistics for current–voltage hysteresis for the parameter set listed in appendix B. The scan rates showing maximum hysteresis factor under the Boltzmann approximation and Fermi–Dirac statistics are plotted in the top-left and top-right panels respectively.

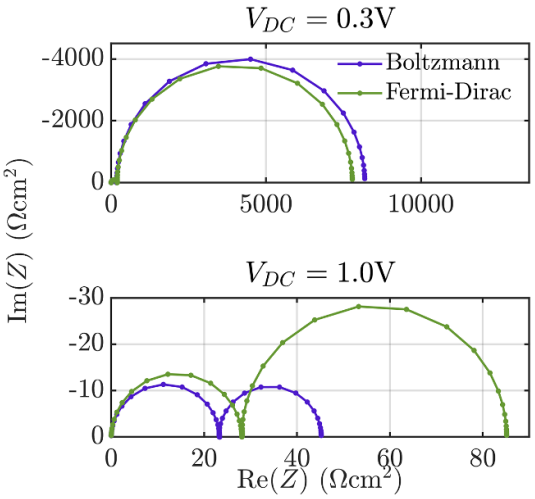

Figure 8. The effect of the Boltzmann approximation vs. full Fermi–Dirac statistics on impedance spectra for the parameter set listed in appendix B. The DC voltages were 0.3 V (top) and 1.0 V (bottom).

A 180 mV s^{-1} scan of the TiO_2/MAPI/Spiro-MeOTAD parameter set shows that the use of Boltzmann statistics in the TLs leads not only to a different open-circuit voltage to that predicted by FD statistics, but also to qualitative differences in the shape of the hysteresis curve and the fill factor obtained from each direction of the scan. It has long been understood that the observed performance of a PSC during a current–voltage sweep is highly influenced by the preconditioning procedure [8], where the cell is held to equilibrate at a high applied voltage. Changes to the statistical integrals strongly influence the preconditioned state of the cell, and thus have a knock-on effect on the predicted performance observed during the sweep. Once again, the shape of the hysteresis curve is highly sensitive to many material parameters and subtleties of the drift–diffusion model and the effects seen for this parameter set cannot be assumed to be uniform across all other parameter sets.

5.3. Impedance spectroscopy

Current–voltage sweeps constitute only one of many dynamic characterisation techniques commonly simulated by drift–diffusion models. Another is IS, in which the steady state is perturbed by a small-amplitude oscillating voltage at varying frequencies and the amplitude and phase of the current response is measured as a function of frequency. This technique can be used to diagnose performance losses and degradation as well as probe the timescales on which the physical processes within the cell operate [13, 111–113]. Recent additions of FD statistics and an IS simulation capability to `IonMonger` [110] provide the first PSC modelling software capable of exploring the interdependent effects of the two. As shown in figure 8, predicted impedance spectra are highly sensitive to changes in the statistical integrals. The discrepancies between the simulations employing the Boltzmann approximation in the TLs and those based on FD statistics in the TLs are exacerbated for larger values of the DC voltage, the value about which the voltage is perturbed, and particularly impact the low-frequency arc, caused by the charging and discharging of the Debye layers and mediated by the mobile ions in the perovskite [13].

6. Conclusion

While the Boltzmann approximation (from which the CER, is derived) has been widely employed in semiconductor modelling, it has often been used without due consideration of the validity of the approximation in the scenario in which it is being employed. Specifically, the use of organic materials to fabricate PSC TLs, and the high doping levels in these structures, suggest that the Boltzmann approximation (22) to the FD statistical distribution (9) (and thus also the CER) is frequently inaccurate in the TLs. This, in turn, can lead to significant errors in the predictions made by PSC charge transport models.

Incorporating a full statistical treatment of the charge carrier dynamics in the TLs (equivalent to using the GER) leads to a density-dependent diffusion enhancement function, Δ, that is determined by the DoS function. For cases in which the Boltzmann approximation is accurate, the diffusion enhancement function reduces to $\Delta = 1$. Crucially, however, the function is highly sensitive to the choice of DoS function. In particular, the region of validity of the Boltzmann approximation depends sensitively on the exact DoS employed by the model. Of the common PSC TL materials, disordered organic materials, which are usually modelled by a Gaussian DoS function, are those for which the Boltzmann approximation is least accurate, due to the diffuse nature of the Gaussian. The accuracy is particularly poor for the materials with greatest disorder, such as PCBM and PEDOT:PSS.

In order to test the sensitivity of drift–diffusion models of a typical TiO_2/MAPI/Spiro-MeOTAD PSC to changes in the description of carrier transport in the TLs of the device, comparison was made between predicted device behaviour obtained from (I) a PSC model in which carrier transport in the TLs was described using the Boltzmann approximation and (II) a PSC model in which full FD statistics were employed.

Numerical solutions show that the the full statistical treatment of carrier transport in the TLs leads to significantly different predictions of four key steady state performance parameters (V_{OC}, J_{SC}, FF and PCE) in comparison to the predictions made by the model in which carrier transport in the TLs is described by the Boltzmann approximation. The most notable is between the predictions of the PCE, the value of which was overestimated by the model based upon the Boltzmann approximation by 27%. This leads us to conclude that the steady state performance of the cell is not well-described by the standard planar PSC model (i.e. one in which the Boltzmann approximation is employed in the TLs). Due to the large number of material parameters in the PSC model and the difficulty in obtaining accurate estimates of their values, it is common to fit some parameters to match experimental data, particularly the four performance parameters considered here. It is clear that fitting these parameters to the standard model (based on the Boltzmann approximation) can easily lead to incorrect predictions of these parameters, and a misleading description of the cell.

In addition to steady state performance, two common dynamic measurements, namely current–voltage hysteresis and IS, were simulated using PSC models based on (I) a Boltzmann description of the TLs and (II) a full FD description of the TLs. For this representative parameter set, the model based on the Boltzmann approximation incorrectly predicts both the maximum hysteresis factor and the scan rate at which this maximum appears (figure 7). Furthermore, the Boltzmann model produces qualitative errors in the shape of the J-V curve across a wide range of physically relevant scan rates. Similar errors were observed in the Boltzmann model when simulating IS, dependent on the DC voltage. At low voltages, carrier densities in the TLs near the perovskite interfaces are lower, meaning the Boltzmann approximation is more likely to be accurate. For greater DC voltages, however, carriers in the TLs accumulate near the perovskite interfaces, affecting the ion vacancy accumulation/depletion occurring on the perovskite side of the interfaces, and thus the low-frequency arc on the Nyquist plot that is caused by ion migration. Recently it has been shown that adopting an asymptotic approach to solving the charge transport model, rather than a numerical one, can

provide significant insight into the IS response of PSCs [112]. Application of these mathematical methods to the modified charge transport model presented here will therefore be the subject of future work, with the aim of elucidating the exact effect of the Boltzmann approximation in IS modelling. The numerical simulations conducted here, however, show that the Boltzmann approximation causes significant errors in predictions of dynamic device-level behaviour.

As understanding of PSC physics continues to improve, it is essential that models of their operation also continue to advance. While PSC drift–diffusion models based on the standard Boltzmann approximation of charge carrier statistics in the TLs may, in some cases, be sufficient, their validity cannot be assumed in general. In particular, while Boltzmann statistics give a fair description of charge transport in weakly doped and inorganic TL materials, they provide a much poorer description of strongly doped and organic TL materials. The numerical methods discussed here, and their implementation in `IonMonger`, give the perovskite community access to fast and accurate numerical models incorporating alternative statistical descriptions of charge carrier behaviour in the TLs that enable simulations of enhanced predictive power, across a wide range of scenarios, which are not solely limited to the steady-state but include current–voltage and IS measurements.

Data availability statement

All data that support the findings of this study are included within the article (and any supplementary files).

Acknowledgment

W C was supported by an EPSRC Grant (reference EP/V520056/1). M W and A B W were supported by the European Commission through the Horizon 2020 Framework Programme for Research and Innovation, Energy Oriented Centre of Excellence (EoCoE-II) project (Grant Agreement ID: 824158).

Appendix A. The full charge transport model

Here we list the full charge transport model of a three-layer PSC, a schematic of which is shown in figure 9. Equations directly modified to account for full FD statistics are highlighted in teal. This charge transport model was presented in [110].

A.1. Perovskite absorber layer ($0 < x < b$)

$$\frac{\partial P}{\partial t} + \frac{\partial F^{\mathrm{p}}}{\partial x} = 0 \qquad F^{\mathrm{p}} = -D_I\left(\frac{\partial P}{\partial x} + \frac{P}{V_{\mathrm{T}}}\frac{\partial \phi}{\partial x}\right) \tag{A1}$$

$$\frac{\partial n}{\partial t} - \frac{1}{q}\frac{\partial j^{\mathrm{n}}}{\partial x} = G(x,t) - R(n,p) \qquad j^{\mathrm{n}} = qD_{\mathrm{n}}\left(\frac{\partial n}{\partial x} - \frac{n}{V_{\mathrm{T}}}\frac{\partial \phi}{\partial x}\right) \tag{A2}$$

$$\frac{\partial p}{\partial t} + \frac{1}{q}\frac{\partial j^{\mathrm{p}}}{\partial x} = G(x,t) - R(n,p) \qquad j^{\mathrm{p}} = -qD_{\mathrm{p}}\left(\frac{\partial p}{\partial x} + \frac{p}{V_{\mathrm{T}}}\frac{\partial \phi}{\partial x}\right) \tag{A3}$$

$$\frac{\partial^2 \phi}{\partial x^2} = \frac{q}{\varepsilon_{\mathrm{A}}}(N_0 - P + n - p) \tag{A4}$$

where G and R are the generation and recombination rates.

A.2. Electron transport layer ($-b_{\mathrm{E}} < x < 0$)

$$\frac{\partial n}{\partial t} - \frac{1}{q}\frac{\partial j^{\mathrm{n}}}{\partial x} = 0 \qquad j^{\mathrm{n}} = \mu_{\mathrm{E}} k_{\mathrm{B}} T n \frac{\partial}{\partial x}\left[\mathcal{S}_{\mathrm{E}}^{-1}\left(\frac{n}{g_{\mathrm{c}}^{\mathrm{E}}}\right) - \frac{\phi}{k_{\mathrm{B}}T}\right] \tag{A5}$$

$$\frac{\partial^2 \phi}{\partial x^2} = \frac{q}{\varepsilon_{\mathrm{E}}}(n - d_{\mathrm{E}}). \tag{A6}$$

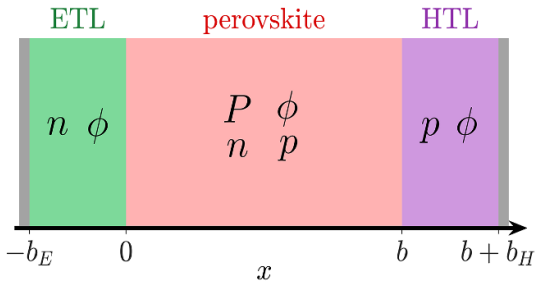

Figure 9. Schematic of the three-layer planar drift–diffusion model of a PSC.

A.3. Hole transport layer ($b < x < b + b_{\mathrm{H}}$)

$$\frac{\partial p}{\partial t} + \frac{1}{q}\frac{\partial j^{\mathrm{p}}}{\partial x} = 0 \qquad j^{\mathrm{p}} = -\mu_{\mathrm{H}} k_{\mathrm{B}} T p \frac{\partial}{\partial x}\left[\mathcal{S}_{\mathrm{H}}^{-1}\left(\frac{p}{g_{\mathrm{v}}^{\mathrm{H}}}\right) + \frac{\phi}{k_{\mathrm{B}}T}\right] \tag{A7}$$

$$\frac{\partial^2 \phi}{\partial x^2} = \frac{q}{\varepsilon_{\mathrm{E}}}(d_{\mathrm{H}} - p). \tag{A8}$$

A.4. Boundary conditions

$$n|_{x=-b_{\mathrm{E}}} = d_{\mathrm{E}}, \qquad \phi|_{x=-b_{\mathrm{E}}} = \frac{V_{bi} - V(t)}{2} \tag{A9}$$

$$p|_{x=b+b_{\mathrm{H}}} = d_{\mathrm{H}}, \qquad \phi|_{x=b+b_{\mathrm{H}}} = -\frac{V_{bi} - V(t)}{2}. \tag{A10}$$

A.5. Continuity conditions

$$\left.\begin{aligned} j^{\mathrm{n}}|_{x=0^-} &= j^{\mathrm{n}}|_{x=0^+} - R_{\mathrm{I}} \\ j^{\mathrm{p}} &= -qR_{\mathrm{I}} \\ F^{\mathrm{p}} &= 0 \\ \phi|_{x=0^-} &= \phi|_{x=0^+} \\ \varepsilon_{\mathrm{E}}\frac{\partial \phi}{\partial x}\Big|_{x=0^-} &= \varepsilon_{\mathrm{A}}\frac{\partial \phi}{\partial x}\Big|_{x=0^+} \\ d_{\mathrm{E}} k_{\mathrm{E}} \exp\left[\mathcal{S}_{\mathrm{E}}^{-1}\left(\frac{n|_{x=0^-}}{g_{\mathrm{c}}^{\mathrm{E}}}\right) - \mathcal{S}_{\mathrm{E}}^{-1}\left(\frac{d_{\mathrm{E}}}{g_{\mathrm{c}}^{\mathrm{E}}}\right)\right] &= n|_{x=0^+} \end{aligned}\right\} \text{on } x = 0 \tag{A11}$$

$$\left.\begin{aligned} j^{\mathrm{p}}|_{x=b^-} - R_{\mathrm{r}} &= j^{\mathrm{p}}|_{x=b^+} \\ j^{\mathrm{n}} &= -qR_{\mathrm{r}} \\ F^{\mathrm{p}} &= 0 \\ \phi|_{x=b^-} &= \phi|_{x=b^+} \\ \varepsilon_{\mathrm{A}}\frac{\partial \phi}{\partial x}\Big|_{x=b^-} &= \varepsilon_{\mathrm{H}}\frac{\partial \phi}{\partial x}\Big|_{x=b^+} \\ p|_{x=b^-} &= d_{\mathrm{H}} k_{\mathrm{H}} \exp\left[\mathcal{S}_{\mathrm{H}}^{-1}\left(\frac{p|_{x=b^+}}{g_{\mathrm{v}}^{\mathrm{H}}}\right) - \mathcal{S}_{\mathrm{H}}^{-1}\left(\frac{d_{\mathrm{H}}}{g_{\mathrm{v}}^{\mathrm{H}}}\right)\right] \end{aligned}\right\} \text{on } x = b \tag{A12}$$

where

$$k_{\mathrm{E}} = \frac{g_{\mathrm{c}}}{d_{\mathrm{E}}} \exp\left(\frac{E_{\mathrm{c}}^{\mathrm{E}} - E_{\mathrm{c}}}{k_{\mathrm{B}}T} + \mathcal{S}_{\mathrm{E}}^{-1}\left(\frac{d_{\mathrm{E}}}{g_{\mathrm{c}}^{\mathrm{E}}}\right)\right) \tag{A13}$$

$$k_{\mathrm{H}} = \frac{g_{\mathrm{v}}}{d_{\mathrm{H}}} \exp\left(\frac{E_{\mathrm{v}} - E_{\mathrm{v}}^{\mathrm{H}}}{k_{\mathrm{B}}T} + \mathcal{S}_{\mathrm{H}}^{-1}\left(\frac{d_{\mathrm{H}}}{g_{\mathrm{v}}^{\mathrm{H}}}\right)\right) \tag{A14}$$

Appendix B. Parameter set

Table 2. Material parameters for a TiO_2/MAPI/spiro-MeOTAD cell. The necessary parameters to model non-Boltzmann statistics in the transport layers are shown in table 1.

Symbol	Name	Values	Unit	References
T	Temperature	298	K	
—	Light entering through	ETL	—	
Perovskite (MAPI)				
b	Perovskite width	400	nm	
ε_p	Permittivity	24.1	ε_0	[114]
α	Absorption coefficient	1.3×10^7	m^{-1}	[115]
g_c	Conduction band effective DoS	8.1×10^{24}	m^{-3}	[114]
g_v	Valence band effective DoS	5.8×10^{24}	m^{-3}	[114]
E_c	Conduction band edge	−3.7	eV	[116]
E_v	Valence band edge	−5.4	eV	[116]
D_n	Electron diffusivity	1.7×10^{-4}	$m^2\ s^{-1}$	[117]
D_p	Hole diffusivity	1.7×10^{-4}	$m^2\ s^{-1}$	[117]
N_0	Mean anion vacancy density	1.6×10^{25}	m^{-3}	[118]
D_P	Anion vacancy diffusivity	1×10^{-17}	$m^2\ s^{-1}$	[9]
ETL (TiO_2)				
g_c^E	Conduction band effective DoS	2×10^{23}	m^{-3}	[81]
E_f^E	Equilibrium electron QFL	−4.19	eV	[119]
D_E	Electron diffusivity	1.3×10^{-5}	$m^2\ s^{-1}$	[120]
ε_E	Permittivity	10	ε_0	
b_E	ETL width	100	nm	[121]
E_c^E	Conduction band edge	−4.13	eV	[84]
HTL (spiro-MeOTAD)				
g_v^H	Valence band effective DoS	1×10^{26}	m^{-3}	[91]
E_f^H	Equilibrium hole QFL	−4.97	eV	
D_H	Hole diffusivity	1×10^{-6}	$m^2\ s^{-1}$	[120]
ε_H	Permittivity	3	ε_0	
b_H	HTL width	200	nm	[121]
E_v^H	Valence band edge	−5.1	eV	[92]

Table 3. Recombination parameters for a typical TiO_2/MAPI/spiro-MeOTAD cell.

Symbol	Name	Values	Unit
Perovskite bulk			
β	Bi-molecular rate constant	1.5×10^{-14}	$m^3\ s^{-1}$
τ_p	Hole SRH psuedo-lifetime	3×10^{-7}	s
τ_n	Electron SRH psuedo-lifetime	3×10^{-7}	s
A_n	Electron Auger coefficient	0	$m^6\ s^{-1}$
A_p	Hole Auger coefficient	0	$m^6\ s^{-1}$
ETL/perovskite interface			
ν_p^E	Hole recombination velocity	10	ms^{-1}
ν_n^E	Electron recombination velocity 0	10^5	ms^{-1}
β_E	Bi-molecular rate constant	0	$m^4\ s^{-1}$
HTL/perovskite interface			
ν_p^H	Hole recombination velocity	10^5	ms^{-1}
ν_n^H	Electron recombination velocity	0.1	ms^{-1}
β_H	Bi-molecular rate constant	0	$m^4\ s^{-1}$

ORCID iDs

Will Clarke https://orcid.org/0000-0002-1629-9698
Matthew J Wolf https://orcid.org/0000-0001-5902-4187
Alison Walker https://orcid.org/0000-0002-2232-9734
Giles Richardson https://orcid.org/0000-0001-6225-8590

References

[1] NREL 2022 Best research-cell efficiency chart (available at: www.nrel.gov/pv/cell-efficiency.html)

[2] Tessler N and Vaynzof Y 2020 Insights from device modeling of perovskite solar cells *ACS Energy Lett.* **5** 1260–70
[3] Le Corre V M, Wang Z, Anton Koster L J and Tress W 2020 Device modeling of perovskite solar cells: insights and outlooks *Soft-Matter Thin Film Solar Cells* (New York: AIP Publishing) pp 1–32
[4] Riquelme A J, Valadez-Villalobos K, Boix P P, Oskam G, Mora-Seró Ivan and Anta J A 2022 Understanding equivalent circuits in perovskite solar cells. insights from drift-diffusion simulation *Phys. Chem. Chem. Phys.* **24** 15657–71
[5] Zhao P, Jie S, Lin Z, Wang J, Zhang J, Hao Y, Ouyang X and Chang J 2020 The crystal anisotropy effect of $MAPbI_3$ perovskite on optoelectronic devices *Mater. Today Energy* **17** 100481
[6] Hameed Khattak Y, Baig F, Shuja A, Atourki L, Riaz K and Marí Soucase Be 2021 Device optimization of pin structured perovskite solar cells: impact of design variants *ACS Appl. Electron. Mater.* **3** 3509–20
[7] Kanoun A-A, Goumri-Said S and Benali Kanoun M 2021 Device design for high-efficiency monolithic two-terminal, four-terminal mechanically stacked and four-terminal optically coupled perovskite-silicon tandem solar cells *Int. J. Energy Res.* **45** 10538–45
[8] Richardson G, O'Kane S E J, Niemann R G, Peltola T A, Foster J M, Cameron P J and Walker A B 2016 Can slow-moving ions explain hysteresis in the current–voltage curves of perovskite solar cells? *Energy Environ. Sci.* **9** 1476–85
[9] Eames C, Frost J M, Barnes P R F, O'Regan B C, Walsh A and Islam M S 2015 Ionic transport in hybrid lead iodide perovskite solar cells *Nat. Commun.* **6** 7497
[10] Bertoluzzi L, Boyd C C, Rolston N, Jixian X, Prasanna R, O'Regan B C and McGehee M D 2020 Mobile ion concentration measurement and open-access band diagram simulation platform for halide perovskite solar cells *Joule* **4** 109–27
[11] Liu M, Johnston M B and Snaith H J 2013 Efficient planar heterojunction perovskite solar cells by vapour deposition *Nature* **501** 395–8
[12] Neukom M T *et al* 2019 Consistent device simulation model describing perovskite solar cells in steady-state, transient and frequency domain *ACS Appl. Mater. Interfaces* **11** 23320–8
[13] Riquelme A, Bennett L J, Courtier N E, Wolf M J, Contreras-Bernal L, Walker A B, Richardson G and Anta J A 2020 Identification of recombination losses and charge collection efficiency in a perovskite solar cell by comparing impedance response to a drift-diffusion model *Nanoscale* **12** 17385–98
[14] Calado P, Telford A M, Bryant D, Xiaoe Li, Nelson J, O'Regan B C and Barnes P R F 2016 Evidence for ion migration in hybrid perovskite solar cells with minimal hysteresis *Nat. Commun.* **7** 13831
[15] Ball J M, Lee M M, Hey A and Snaith H J 2013 Low-temperature processed meso-superstructured to thin-film perovskite solar cells *Energy Environ. Sci.* **6** 1739
[16] Docampo P, Ball J M, Darwich M, Eperon G E and Snaith H J 2013 Efficient organometal trihalide perovskite planar-heterojunction solar cells on flexible polymer substrates *Nat. Commun.* **4** 2761
[17] Van Reenen S, Kemerink M and Snaith H J 2015 Modeling anomalous hysteresis in perovskite solar cells *J. Phys. Chem. Lett.* **6** 3808–14
[18] Courtier N E, Richardson G and Foster J M 2018 A fast and robust numerical scheme for solving models of charge carrier transport and ion vacancy motion in perovskite solar cells *Appl. Math. Modelling* **63** 329–48
[19] Courtier N E, Foster J M, O'Kane S E J, Walker A B and Richardson G 2019 Systematic derivation of a surface polarisation model for planar perovskite solar cells *Eur. J. Appl. Math.* **30** 427–57
[20] Courtier N E, Cave J M, Foster J M, Walker A B and Richardson G 2019 How transport layer properties affect perovskite solar cell performance: insights from a coupled charge transport/ion migration model *Energy Environ. Sci.* **12** 396–409
[21] Courtier N E, Cave J M, Walker A B, Richardson G and Foster J M 2019 Ionmonger: a free and fast planar perovskite solar cell simulator with coupled ion vacancy and charge carrier dynamics *J. Comput. Electron.* **18** 1435–49
[22] Calado P, Gelmetti I, Hilton B, Azzouzi M, Nelson J and Barnes P R F 2022 Driftfusion: an open source code for simulating ordered semiconductor devices with mixed ionic-electronic conducting materials in one dimension *J. Comput. Electron.* **21** 137–52
[23] Azri F, Meftah A, Sengouga N and Meftah A 2019 Electron and hole transport layers optimization by numerical simulation of a perovskite solar cell *Sol. Energy* **181** 372–8
[24] Hima A, Lakhdar N, Benhaoua B, Saadoune A, Kemerchou I and Rogti F 2019 An optimized perovskite solar cell designs for high conversion efficiency *Superlattices Microstruct.* **129** 240–6
[25] Markowich P A, Ringhofer C A and Schmeiser C 2012 *Semiconductor Equations* (Vienna: Springer Science & Business Media)
[26] Landsberg P T 1981 Einstein and statistical thermodynamics. III. The diffusion-mobility relation in semiconductors *Eur. J. Phys.* **2** 213
[27] Ashcroft N W and Mermin N D 1976 *Solid State Physics* vol 1 (Saunders College Publishing) p 2
[28] Roichman Y and Tessler N 2002 Generalized einstein relation for disordered semiconductors–implications for device performance *Appl. Phys. Lett.* **80** 1948–50
[29] Pasveer W F, Cottaar J, Tanase C, Coehoorn R, Bobbert P A, Blom P W M, de Leeuw D M and Michels M A J 2005 Unified description of charge-carrier mobilities in disordered semiconducting polymers *Phys. Rev. Lett.* **94** 206601
[30] Sun J-X, Yang H-C, Yang Li and Cui H-J 2021 Unified mobility model for diffusion-limited current in organic diodes based on Fermi-Dirac statistics *Phys. Rev. Appl.* **16** 034037
[31] Nenashev A V, Oelerich J O, Dvurechenskii A V, Gebhard F and Baranovskii S D 2017 Fundamental characteristic length scale for the field dependence of hopping charge transport in disordered organic semiconductors *Phys. Rev.* B **96** 035204
[32] Alvarez A O, Arcas Ron, Aranda C A, Bethencourt L, Mas-Marzá E, Saliba M and Fabregat-Santiago F 2020 Negative capacitance and inverted hysteresis: matching features in perovskite solar cells *J. Phys. Chem. Lett.* **11** 8417–23
[33] Hermes I M, Hou Y, Bergmann V W, Brabec C J and Weber S A L 2018 The interplay of contact layers: how the electron transport layer influences interfacial recombination and hole extraction in perovskite solar cells *J. Phys. Chem. Lett.* **9** 6249–56
[34] Kerner R A and Rand B P 2017 Linking chemistry at the $TiO_2CH_3NH_3PbI_3$ interface to current–voltage hysteresis *J. Phys. Chem. Lett.* **8** 2298–303
[35] Egger D A, Bera A, Cahen D, Hodes G, Kirchartz T, Kronik L, Lovrincic R, Rappe A M, Reichman D R and Yaffe O 2018 What remains unexplained about the properties of halide perovskites? *Adv. Mater.* **30** 1800691
[36] Novikov S V, Dunlap D H, Kenkre V M, Parris P E and Vannikov A V 1998 Essential role of correlations in governing charge transport in disordered organic materials *Phys. Rev. Lett.* **81** 4472–5
[37] Bässler H 1993 Charge transport in disordered organic photoconductors. A monte carlo simulation study *Phys. Status Solidi* b **175** 1

[38] Tessler N and Roichman Y 2005 Amorphous organic molecule/polymer diodes and transistors–comparison between predictions based on Gaussian or exponential density of states *Org. Electron.* **6** 200–10
[39] Abdel D, Vágner P, Fuhrmann Jurgen and Farrell P 2021 Modelling charge transport in perovskite solar cells: potential-based and limiting ion depletion *Electrochim. Acta* **390** 138696
[40] Abdel D, Courtier N and Farrell P 2022 Volume exclusion effects in perovskite charge transport modeling *2022 Int. Conf. on Numerical Simulation of Optoelectronic Devices (NUSOD)* (IEEE) pp 107–8
[41] Jacoboni C 2010 *Theory of Electron Transport in Semiconductors: a Pathway From Elementary Physics to Nonequilibrium Green Functions* vol 165 (Heidelberg: Springer Science & Business Media)
[42] Grasser T, Tang T W, Kosina H and Selberherr S 2003 A review of hydrodynamic and energy-transport models for semiconductor device simulation *Proc. IEEE* **91** 251–74
[43] Hwang I, McNeill C R and Greenham N C 2009 Drift-diffusion modeling of photocurrent transients in bulk heterojunction solar cells *J. Appl. Phys.* **106** 094506
[44] Koster L J A, Smits E C P, Mihailetchi V D and Blom P W M 2005 Device model for the operation of polymer/fullerene bulk heterojunction solar cells *Phys. Rev.* B **72** 085205
[45] Foster J M, Snaith H J, Leijtens T and Richardson G 2014 A model for the operation of perovskite based hybrid solar cells: formulation, analysis and comparison to experiment *SIAM J. Appl. Math.* **74** 1935–66
[46] Van Mensfoort S L M and Coehoorn R 2008 Effect of Gaussian disorder on the voltage dependence of the current density in sandwich-type devices based on organic semiconductors *Phys. Rev.* B **78** 085207
[47] Patriarca M, Farrell P, Fuhrmann Jurgen and Koprucki T 2019 Highly accurate quadrature-based Scharfetter–Gummel schemes for charge transport in degenerate semiconductors *Comput. Phys. Commun.* **235** 40–49
[48] Abdel D, Farrell P and Fuhrmann Jurgen 2021 Assessing the quality of the excess chemical potential flux scheme for degenerate semiconductor device simulation *Opt. Quantum Electron.* **53** 163
[49] Koprucki T, Rotundo N, Farrell P, Hai Doan D and Fuhrmann Jurgen 2015 On thermodynamic consistency of a Scharfetter–Gummel scheme based on a modified thermal voltage for drift-diffusion equations with diffusion enhancement *Opt. Quantum Electron.* **47** 1327–32
[50] Koprucki T and Gärtner K 2013 Discretization scheme for drift-diffusion equations with strong diffusion enhancement *Opt. Quantum Electron.* **45** 791–6
[51] Troisi A and Orlandi G 2006 Dynamics of the intermolecular transfer integral in crystalline organic semiconductors *J. Phys. Chem.* A **110** 4065–70
[52] Ciuchi S, Fratini S and Mayou D 2011 Transient localization in crystalline organic semiconductors *Phys. Rev.* B **83** 081202(R)
[53] Fishchuk I I, Kadashchuk A, Bhoolokam A, de Jamblinne de Meux A, Pourtois G, Gavrilyuk M M, Köhler A, Bässler H, Heremans P and Genoe J 2016 Interplay between hopping and band transport in high-mobility disordered semiconductors at large carrier concentrations: the case of the amorphous oxide InGaZnO *Phys. Rev.* B **93** 195204
[54] Oberhofer H, Reuter K and Blumberger J 2017 Charge transport in molecular materials: an assessment of computational methods *Chem. Rev.* **117** 10319–57
[55] Nelson J A 2003 *The Physics of Solar Cells* (London: Imperial College Press)
[56] Kim R, Wang X and Lundstrom M 2008 Notes on Fermi-Dirac integrals (arXiv:0811.0116)
[57] Kane E O 1957 Band structure of indium antimonide *J. Phys. Chem. Solids* **1** 249–61
[58] Ehrenreich H 1960 Band structure and electron transport of gaas *Phys. Rev.* **120** 1951
[59] Conwell E M and Vassell M O 1968 High-field transport in n-type gaas *Phys. Rev.* **166** 797
[60] Paasch G and Scheinert S 2010 Charge carrier density of organics with Gaussian density of states: analytical approximation for the Gauss–Fermi integral *J. Appl. Phys.* **107** 104501
[61] Zhou H *et al* 2014 Interface engineering of highly efficient perovskite solar cells *Science* **345** 542–6
[62] Arafat Mahmud Md, Elumalai N K, Upama M B, Wang D, Chan K H, Wright M, Xu C, Haque F and Uddin A 2017 Low temperature processed ZnO thin film as electron transport layer for efficient perovskite solar cells *Sol. Energy Mater. Sol. Cells* **159** 251–64
[63] Cao J, Wu B, Chen R, Wu Y, Hui Y, Mao B-W and Zheng N 2018 Efficient, hysteresis-free and stable perovskite solar cells with ZnO as electron-transport layer: effect of surface passivation *Adv. Mater.* **30** 1705596
[64] Jung K-H, Seo J-Y, Lee S, Shin H and Park N-G 2017 Solution-processed SnO_2 thin film for a hysteresis-free planar perovskite solar cell with a power conversion efficiency of 19.2% *J. Mater. Chem.* A **5** 24790–803
[65] Zhang M, Fengmin W, Chi D, Shi K and Huang S 2020 High-efficiency perovskite solar cells with poly(vinylpyrrolidone)-doped SnO_2 as an electron transport layer *Mater. Adv.* **1** 617–24
[66] Islam M B, Yanagida M, Shirai Y, Nabetani Y and Miyano K 2017 NiOx hole transport layer for perovskite solar cells with improved stability and reproducibility *ACS Omega* **2** 2291–9
[67] Zijun H, Chen D, Yang P, Yang L, Qin L, Huang Y and Zhao X 2018 Sol-gel-processed yttrium-doped NiO as hole transport layer in inverted perovskite solar cells for enhanced performance *Appl. Surf. Sci.* **441** 258–64
[68] Hawash Z, Ono L K and Yabing Q 2018 Recent advances in Spiro-MeOTAD hole transport material and its applications in organic–inorganic halide perovskite solar cells *Adv. Mater. Interfaces* **5** 1700623
[69] Ganesan P, Fu K, Gao P, Raabe I, Schenk K, Scopelliti R, Luo J, Wong L H, Grätzel M and Nazeeruddin M K 2015 A simple spiro-type hole transporting material for efficient perovskite solar cells *Energy Environ. Sci.* **8** 1986–91
[70] Mamun Reza K *et al* 2020 Tailored PEDOT: PSS hole transport layer for higher performance in perovskite solar cells: enhancement of electrical and optical properties with improved morphology *J. Energy Chem.* **44** 41–50
[71] Xia Y and Dai S 2021 Review on applications of PEDOTs and PEDOT:PSS in perovskite solar cells *J. Mater. Sci., Mater. Electron.* **32** 12746–57
[72] Niu J, Yang D, Ren X, Yang Z, Liu Y, Zhu X, Zhao W and Liu S 2017 Graphene-oxide doped PEDOT: PSS as a superior hole transport material for high-efficiency perovskite solar cell *Org. Electron.* **48** 165–71
[73] Hyuk Jung E, Joong Jeon N, Young Park E, Su Moon C, Joo Shin T, Yang T-Y, Hong Noh J and Seo J 2019 Efficient, stable and scalable perovskite solar cells using poly(3-hexylthiophene) *Nature* **567** 511–5
[74] Zhou P, Bu T, Shi S, Li L, Zhang Y, Ku Z, Peng Y, Zhong J, Cheng Y-B and Huang F 2018 Efficient and stable mixed perovskite solar cells using P3HT as a hole transporting layer *J. Mater. Chem.* **6** 5733–7
[75] Liu X, Xia X, Cai Q, Cai F, Yang L, Yan Y and Wang T 2017 Efficient planar heterojunction perovskite solar cells with weak hysteresis fabricated via bar coating *Sol. Energy Mater. Sol. Cells* **159** 412–7

[76] Bai Y, Yu H, Zhu Z, Jiang K, Zhang T, Zhao N, Yang S and Yan H 2015 High performance inverted structure perovskite solar cells based on a PCBM:polystyrene blend electron transport layer *J. Mater. Chem.* A **3** 9098–102
[77] Pitchaiya S, Natarajan M, Santhanam A, Asokan V, Yuvapragasam A, Madurai Ramakrishnan V, Palanisamy S E, Sundaram S and Velauthapillai D 2020 A review on the classification of organic/inorganic/carbonaceous hole transporting materials for perovskite solar cell application *Arab. J. Chem.* **13** 2526–57
[78] Zheng S, Wang G, Liu T, Lou L, Xiao S and Yang S 2019 Materials and structures for the electron transport layer of efficient and stable perovskite solar cells *Sci. China Chem.* **62** 800–9
[79] Jesper Jacobsson T *et al* 2022 An open-access database and analysis tool for perovskite solar cells based on the fair data principles *Nat. Energy* **7** 107–15
[80] Hsiao K-C, Jao M-H, Tian K-Y, Lin T-H, Tran D-P, Liao H-C, Hou C-H, Shyue J-J, Wu M-C and Su W-F 2020 Acetamidinium cation to confer ion immobilization and structure stabilization of organometal halide perovskite toward long life and high-efficiency p-i-n planar solar cell via air-processable method *Sol. RRL* **4** 2000197
[81] Mouchou R T, Jen T C, Laseinde O T and Ukoba K O 2021 Numerical simulation and optimization of p-NiO/n-TiO_2 solar cell system using SCAPS *Mater. Today Proc.* **38** 835–41
[82] Zhang B, Su J, Guo X, Zhou L, Lin Z, Feng L, Zhang J, Chang J and Hao Y 2020 NiO/perovskite heterojunction contact engineering for highly efficient and stable perovskite solar cells *Adv. Sci.* **7** 1903044
[83] Jeong M *et al* 2020 Stable perovskite solar cells with efficiency exceeding 24.8% and 0.3V voltage loss *Science* **369** 1615–20
[84] Malekshahi Byranvand M *et al* 2018 p-type CuI islands on TiO_2 electron transport layer for a highly efficient planar-perovskite solar cell with negligible hysteresis *Adv. Energy Mater.* **8** 1702235
[85] Dong X, Chen D, Zhou J, Zheng Y-Z and Tao X 2018 High crystallization of a multiple cation perovskite absorber for low-temperature stable ZnO solar cells with high-efficiency of over 20% *Nanoscale* **10** 7218–27
[86] Yue M, Su J, Zhao P, Lin Z, Zhang J, Chang J and Hao Y 2019 Optimizing the performance of CsPbI3-based perovskite solar cells via doping a ZnO electron transport layer coupled with interface engineering *Nano-Micro Lett.* **11** 91
[87] Sun Y, Wang W, Zhang H, Su Q, Wei J, Liu P, Chen S and Zhang S 2018 High-performance quantum dot light-emitting diodes based on Al-doped ZnO nanoparticles electron transport layer *ACS Appl. Mater. Interfaces* **10** 18902–9
[88] Yoo J J *et al* 2021 Efficient perovskite solar cells via improved carrier management *Nature* **590** 587–93
[89] Zhao P, Lin Z, Wang J, Yue M, Su J, Zhang J, Chang J and Hao Y 2019 Numerical simulation of planar heterojunction perovskite solar cells based on SnO_2 electron transport layer *ACS Appl. Energy Mater.* **2** 4504–12
[90] Wang Di, Chen S-Ci and Zheng Q 2019 Poly(vinylpyrrolidone)-doped SnO_2 as an electron transport layer for perovskite solar cells with improved performance *J. Mater. Chem.* **7** 12204–10
[91] Peterson K A, Patterson A, Vega-Flick A, Liao B and Chabinyc M L 2020 Doping molecular organic semiconductors by diffusion from the vapor phase *Mater. Chem. Front.* **4** 3632–9
[92] Chi W-J, Quan-Song Li and Ze-Sheng Li 2016 Exploring the electrochemical properties of hole transport materials with spiro-cores for efficient perovskite solar cells from first-principles *Nanoscale* **8** 6146–54
[93] Kirkpatrick J and Nelson J 2005 Theoretical study of the transfer integral and density of states in spiro-linked triphenylamine derivatives *J. Chem. Phys.* **123** 084703
[94] Sallenave X, Shasti M, Anaraki E H, Volyniuk D, Grazulevicius J V, Zakeeruddin S M, Mortezaali A, Grätzel M, Hagfeldt A and Sini G 2020 Interfacial and bulk properties of hole transporting materials in perovskite solar cells: spiro-MeTAD versus spiro-OMeTAD *J. Mater. Chem.* A **8** 8527–39
[95] Ilhan Y and Houk K N 2017 Mesoscale ordering and charge-transport of crystalline Spiro-OMeTAD organic semiconductors *J. Phys. Chem.* C **121** 993–9
[96] Wang K, Zheng L, Zhu T, Yao X, Yi C, Zhang X, Cao Y, Liu L, Hu W and Gong X 2019 Efficient perovskite solar cells by hybrid perovskites incorporated with heterovalent neodymium cations *Nano Energy* **61** 352–60
[97] Kuan-Ying H, Li C-K, Syu H-J, Lai Y, Lin C-F and Wu Y-R 2016 Analysis of the PEDOT:PSS/Si nanowire hybrid solar cell with a tail state model *J. Appl. Phys.* **120** 215501
[98] Hwang J, Amy F and Kahn A 2006 Spectroscopic study on sputtered PEDOT/PSS: role of surface PSS layer *Org. Electron.* **7** 387–96
[99] Whitcher T J, Wong W S, Talik A N, Woon K L, Chanlek N, Nakajima H, Saisopa T and Songsiriritthigul P 2016 Investigation into the Gaussian density of states widths of organic semiconductors *J. Phys. D: Appl. Phys.* **49** 325106
[100] Min H, Kim M, Lee S-U, Kim H, Kim G, Choi K, Lee J H and Seok S I 2019 Efficient, stable solar cells by using inherent bandgap of α-phase formamidinium lead iodide *Science* **366** 749–53
[101] Mackenzie R C I, Kirchartz T, Dibb G F A and Nelson J 2011 Modeling nongeminate recombination in P3HT:PCBM solar cells *J. Phys. Chem.* C **115** 9806–13
[102] Kanai Y and Jeffrey C G 2008 Role of semiconducting and metallic tubes in P3HT/carbon-nanotube photovoltaic heterojunctions: density functional theory calculations *Nano Lett.* **8** 908–12
[103] Wenzhan X, Zheng L, Zhang X, Cao Y, Meng T, Wu D, Liu L, Hu W and Gong X 2018 Efficient perovskite solar cells fabricated by Co partially substituted hybrid perovskite *Adv. Energy Mater.* **8** 1703178
[104] Garcia-Belmonte Gà, Boix P P, Bisquert J, Sessolo M and Bolink H J 2010 Simultaneous determination of carrier lifetime and electron density-of-states in P3HT: PCBM organic solar cells under illumination by impedance spectroscopy *Sol. Energy Mater. Sol. Cells* **94** 366–75
[105] Mihailetchi V D *et al* 2003 Electron transport in a methanofullerene *Adv. Funct. Mater.* **13** 43–46
[106] Steiner F, Foster S, Losquin A, Labram J, Anthopoulos T D, Frost J M and Nelson J 2015 Distinguishing the influence of structural and energetic disorder on electron transport in fullerene multi-adducts *Mater. Horiz.* **2** 113–9
[107] Mikroyannidis J A, Kabanakis A N, Sharma S S and Sharma G D 2011 A simple and effective modification of PCBM for use as an electron acceptor in efficient bulk heterojunction solar cells *Adv. Funct. Mater.* **21** 746–55
[108] Horowitz G 2015 Validity of the concept of band edge in organic semiconductors *J. Appl. Phys.* **118** 115502
[109] Castro-Chong A, Riquelme A J, Aernouts T, Bennett L J, Richardson G, Oskam G and Anta J A 2021 Illumination intensity dependence of the recombination mechanism in mixed perovskite solar cells *ChemPlusChem* **86** 1347–56
[110] Clarke W, Bennett L J, Grudeva Y, Foster J M, Richardson G and Courtier N E 2022 Ionmonger 2.0: software for free, fast and versatile simulation of current, voltage and impedance response of planar perovskite solar cells *J. Comput. Electron.* **22** 364–82
[111] Pockett A, Eperon G E, Sakai N, Snaith H J, Peter L M and Cameron P J 2017 Microseconds, milliseconds and seconds: deconvoluting the dynamic behaviour of planar perovskite solar cells *Phys. Chem. Chem. Phys.* **19** 5959–70
[112] Bennett L J, Riquelme A J, Anta J A, Courtier N E and Richardson G 2023 Avoiding ionic interference in computing the ideality factor for perovskite solar cells and an analytical theory of their impedance-spectroscopy response *Phys. Rev. Appl.* **19** 014061

[113] Orazem M E and Tribollet B 2008 *Electrochemical Impedance Spectroscopy* (New York: Wiley) pp 383–9
[114] Brivio F, Butler K T, Walsh A and Van Schilfgaarde M 2014 Relativistic quasiparticle self-consistent electronic structure of hybrid halide perovskite photovoltaic absorbers *Phys. Rev.* B **89** 155204
[115] Löper P *et al* 2015 Complex refractive index spectra of $CH_3NH_3PbI_3$ perovskite thin films determined by spectroscopic ellipsometry and spectrophotometry *J. Phys. Chem. Lett.* **6** 66–71
[116] Schulz P *et al* 2014 Interface energetics in organo-metal halide perovskite-based photovoltaic cells *Energy Environ. Sci.* **7** 1377
[117] Stoumpos C C, Malliakas C D and Kanatzidis M G 2013 Semiconducting tin and lead iodide perovskites with organic cations: phase transitions, high mobilities and near-infrared photoluminescent properties *Inorg. Chem.* **52** 9019–38
[118] Futscher M H, Lee J M, McGovern L, Muscarella L A, Wang T, Haider M I, Fakharuddin A, Schmidt-Mende L and Ehrler B 2019 Quantification of ion migration in $CH_3NH_3PbI_3$ perovskite solar cells by transient capacitance measurements *Mater. Horiz.* **6** 1497–503
[119] Zhe X, Jihuai W, Tongyue W, Bao Q, Xin H, Lan Z, Lin J, Huang M, Huang Y and Fan L 2017 Tuning the Fermi level of TiO_2 electron transport layer through europium doping for highly efficient perovskite solar cells *Energy Technol.* **5** 1820–6
[120] Wang H *et al* 2012 Effect of growth temperature on structure and optical characters of NiO films fabricated by PA-MOCVD *Vacuum* **86** 2044–7
[121] Xia G, Huang B, Zhang Y, Zhao X, Wang C, Jia C, Zhao J, Chen W and Jiangyu Li 2019 Nanoscale insights into photovoltaic hysteresis in triple-cation mixed-halide perovskite: Resolving the role of polarization and ionic migration *Adv. Mater.* **31** 1902870